In-plane fracture analysis of paperboard using x-ray tomography

Master's Dissertation by

Daniel Andersson
Olof Hedberg

Supervisors:
Adjunct Professor Johan Tryding, Tetra Pak®
Associate Professor Stephen Hall, Div. of Solid Mechanics

Examiner:
Professor Matti Ristinmaa, Div. of Solid Mechanics

Acknowledgements

Abstract

In this Master's Thesis x-ray tomography was used during tensile experiments on paperboard to study delamination and cohesive failure. Digital volume correlation of the x-ray tomograph images enabled quantitative analysis of strain fields.

Tensile experiments on different specimen geometries were also conducted to investigate how the geometry affected the response of the specimens during loading. By analysing the size effects and by using normalisation it was found that the behaviour of the material during tensile experiments was independent of the geometry. Using x-ray tomography images, a thickness increase was measured, all the way from loading start to sample failure. It was found that right before the failure strength, the material experienced a higher dilation compared to during the rest of the experiment. It was further found, using digital volume correlation, that the normal strains in the loading direction localised in parabolic zones with higher strains between the notches in the test sample. From the shear strain fields it was also noted that in close proximity to the failure strength, shear strains increased.

The thickness increase right before failure was probably caused by delamination of the paperboard. However, even though delamination results in dilation of the sample it was proven, by performing tensile tests on pre-delaminated samples, that it does not affect the cohesive failure. This means that delamination does not cause in-plane failure. From the analysis it was instead observed that the in-plane failure occurs at the zones with higher strains in the loading direction.

During this Master's Thesis it was found that the combination of x-ray tomography and digital volume correlation is effective to gain more information about the internal structure and deformation of paperboard.

Contents

CHAPTER 1

Introduction

1.1 Introduction to paperboard

Packages can be constructed from many different materials, for example glass, plastic and paperboard. By using a package that is made out of paperboard, one can achieve a durable package at the same time as it is recyclable. Paperboard has a high strength compared to other materials with the same weight and is relatively cheap which makes it a good material to work with when packages are developed and manufactured [1]. A package consisting of paperboard, to be used for drinks or food, normally consist of several layers of different materials. For aseptic packages the three major components are paperboard, aluminium and polymer. The paperboard gives the package its structure and geometry and the aluminium works as a barrier for sunlight and contaminations. Furthermore, polymer layers are used for sealing the package and is the material that is in direct contact with the filled product. A polymer layer is also used on the outside of the package to increase its water resistance and to achieve a glossy surface. In this Master's Thesis only the paperboard part of the package will be analysed.

During forming of packages, the materials will be subjected to different types of loading, which may damage the package, since the applied loads may lead to crack propagation and delamination. Damages may affect the quality of the package which, in the end, may lead to contamination of the product inside. To avoid damages it is of importance to understand how and why delamination occurs and cracks propagate.

There exists three types of crack opening modes that corresponds to different load cases. These are called Mode I, Mode II and Mode III (Figure 1.1). These modes can also be combined to describe all types of loading scenarios [2].
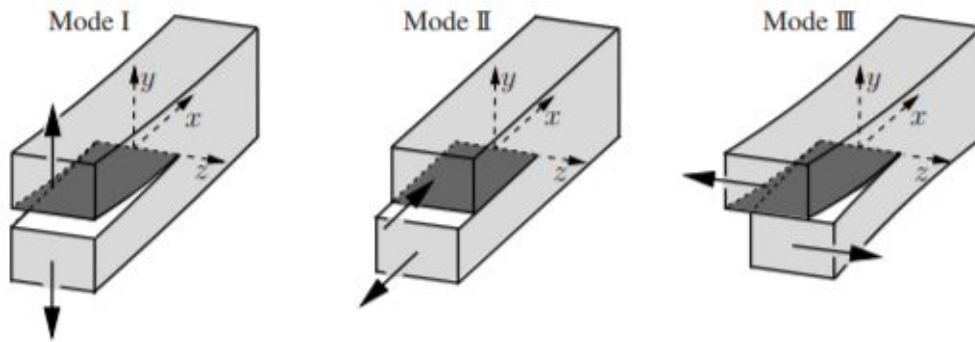
Figure 1.1: Crack opening modes, picture taken from [2].

When a crack initiates, the characteristics of the material can change rapidly. For paperboard, if the crack propagates through the entire sample either the sample breaks into two separate pieces or the crack is widened. The amount of widening of the crack before final rapture is related to loading, geometry and crack size [3]. When analysing crack propagation it is important to know that stress concentrations may occur at places where there are defects in the material. Such defects can, for example, be holes or notches. Sharp defects result in high stress concentrations and should therefore be avoided, if it is desired that the material should carry as much load as possible [4].

Paperboard is composed of a number of cellulose fibres, which together form a fibre network. There are mainly two types of fibres used in paperboard and these originate from softwood or from hardwood. Examples of softwood trees are pine and spruce, while oak and birch are hardwood [5]. The fibre length is normally below 3.6 mm for softwood and below 1.2 mm for hardwood. Many paperboards contain a mix of hardwood and softwood to optimise the production efficiency and functionality [6]. Furthermore, a paperboard may consist of one or multiple plies, where a multiple ply paperboard has layers with different properties stacked on top of each other in the thickness direction.

The direction dependent properties of paperboard have to do with the fibres mainly being aligned in the direction that the machine produces the material. In Figure 1.2 the composition of paper can be seen. The mechanical properties of paperboard depends on the characteristics of the fibre network, such as the alignment of the fibres and the fibre-to-fibre bonds [7]. Since the mechanical properties are direction dependent, paperboard is an anisotropic material. The anisotropy of paperboard is an important property to consider when analysing the material.
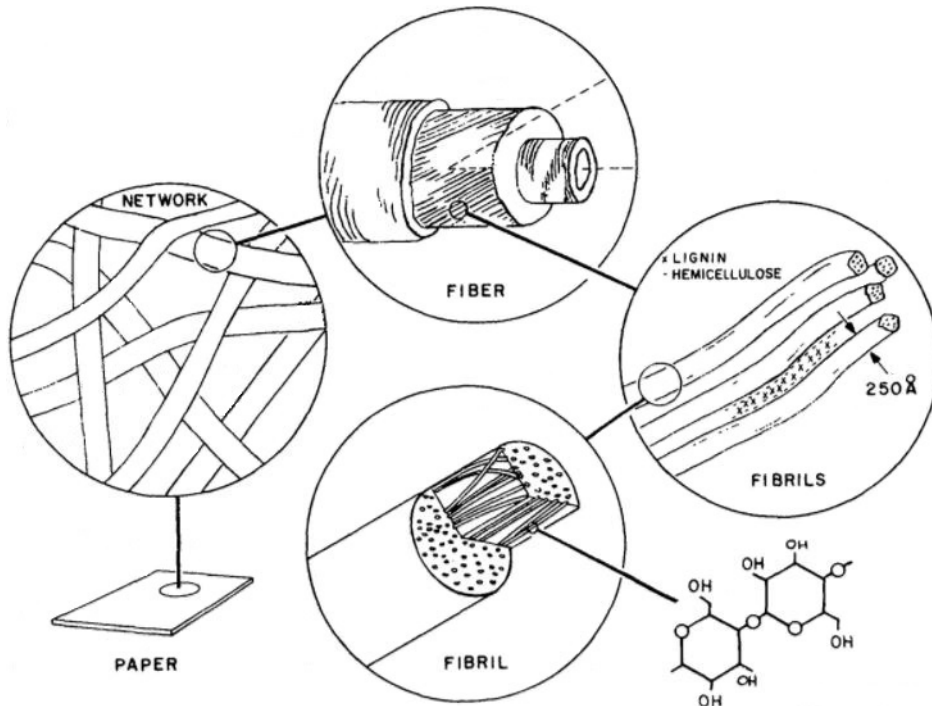
Figure 1.2: Illustration of the composition of paper, picture taken from [8].

In Figure 1.3 a paperboard can be seen including the definitions of different directions. MD stands for Machine Direction, CD stands for Cross Machine Direction, which is 90° offset from the MD direction. ZD is the out-of-plane direction, pointing out of the paperboard, perpendicular to both MD and CD. MD and CD are said to be the in-plane directions while ZD is the out-of-plane direction.
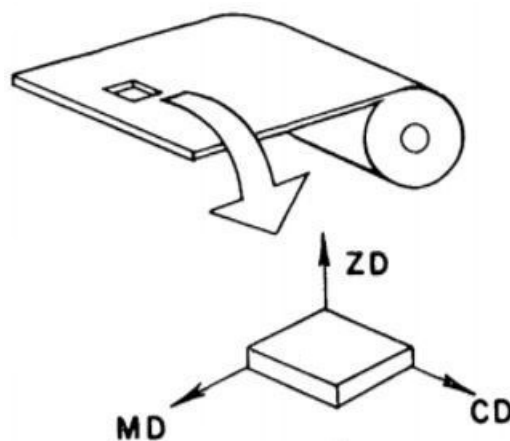
Figure 1.3: Illustration of the different directions of paperboard, picture taken from [8].

Due to the fibre orientation, paperboard has different mechanical properties, e.g. stiffness and failure strength, in different directions. In MD, paperboard is able to handle a stress much larger than in CD and ZD before it breaks. Figure 1.4 shows

3

one stress-displacement curve in MD and one in CD. From this figure it is visible that paperboard has higher strength in MD than in CD. Typically the stiffness in MD is one to five times larger than in CD, and 100 times larger than in ZD [9]. The ZD has the lowest strength and stiffness due to the fact that the fibres are stacked on top of each other in this direction [6].
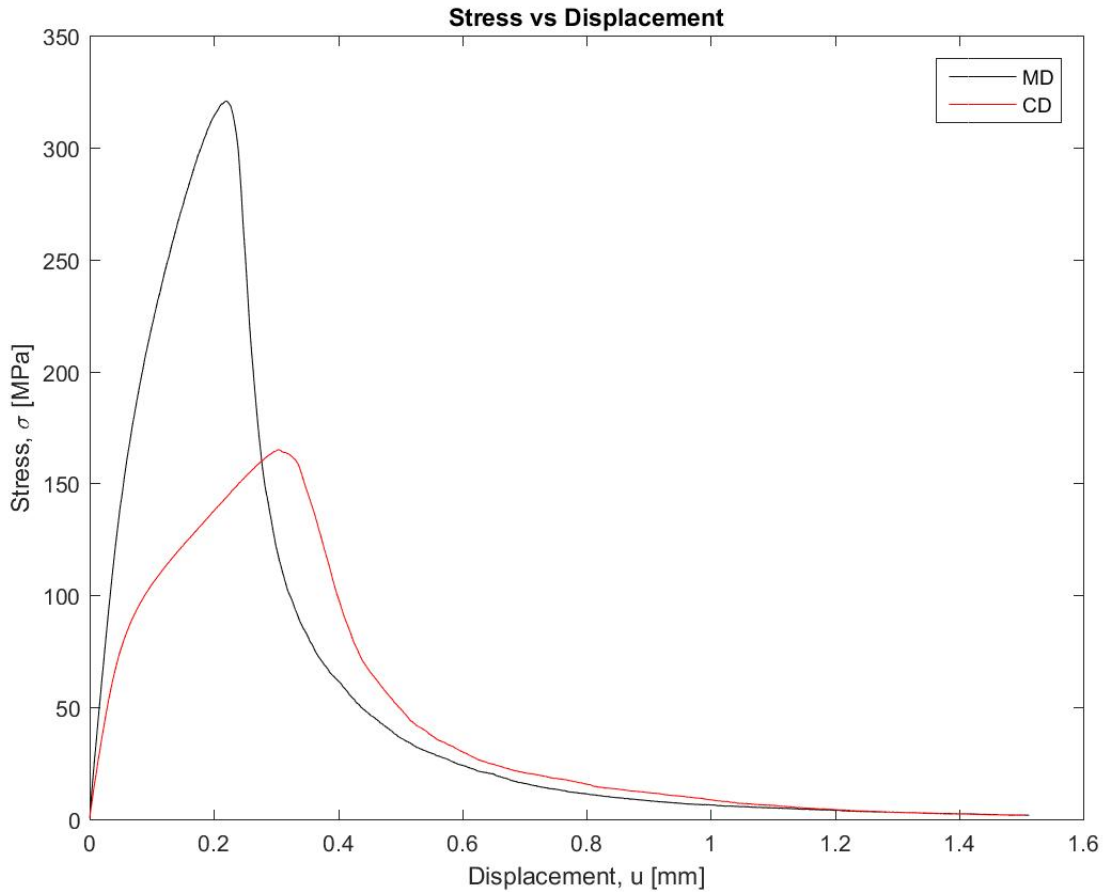
Figure 1.4: Stress-displacement curves for tensile tests performed on paperboard in MD and CD respectively.

1.2   Introduction to x-ray tomography

The microstructure of a material may change over time if it is subjected to an external perturbation. To understand how the microstructure evolves it can be advantageous to be able to study the internal structure of the material. This can be done with x-ray tomography, which is a non-destructive imaging method. The principle of x-ray tomography can be seen in Figure 1.5 and is described below.
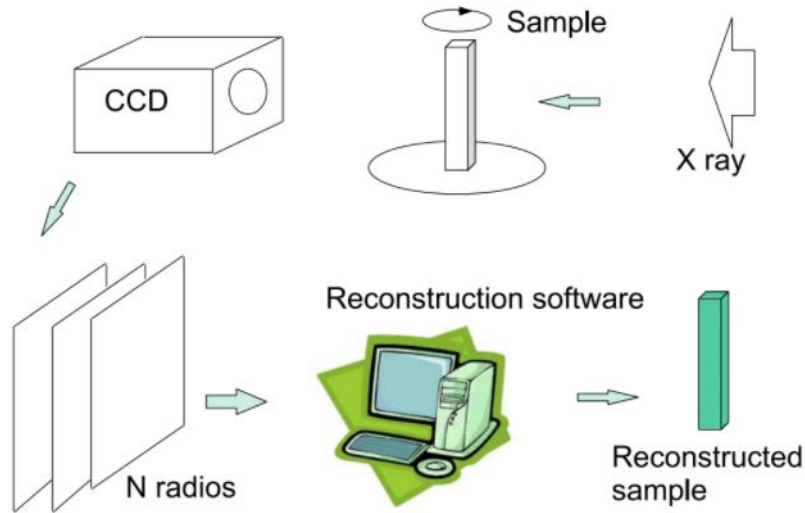
Figure 1.5: The principle of x-ray tomography, where an x-ray is sent from an x-ray source through the sample and hits a detector. Multiple two dimensional images, i.e. radiographs, of the internal structure are then created and reconstructed into a three dimensional image, picture taken from [10].

X-ray tomography involves an x-ray source and an x-ray detector. A system to rotate the study object relative to the source and detector is also needed. X-rays produced at the source pass through the sample and interacts with it such that some of the x-rays are scattered or absorbed. This result in a reduced intensity of the x-ray beam reaching the detector, i.e. the x-rays are attenuated. The attenuation of the x-rays depends on the composition and microstructure of the material. The x-ray detector records a two dimensional image of the x-rays transmitted through the sample. Since the intensity of the beam without the sample is known and the detector has collected the intensity with the sample mounted, the difference in intensity can be determined. The decrease in intensity shows how easy the x-ray beams go through the sample. When this has been done once, the sample is rotated some angle and the intensity is collected again. After this, the attenuation coefficient, which is a measure of how easily the beam passes through the sample can be calculated. The attenuation coefficient throughout the sample can be determined by tomographic reconstruction, as described, for example in [10].

By performing in-situ experiments (i.e. experiments in the tomograph) with x-ray tomography, a series of three dimensional images of the material can be generated. From such image series it is possible to make observations regarding the change in the internal structure of a material during the experiment. For example, it is possible to study how the material behaves when plasticity starts and when cracks occur.

1.3 Aims of this Master's Thesis

To continue the development of paperboard-based packages it is of importance to further analyse the packaging material to gain more knowledge about it. In this Master's Thesis a one ply paperboard has been analysed using tensile experiments and x-ray tomography. This has enabled an analysis of how the paperboard behaves under tensile loading.

The aims of this Master's Thesis were:

- to analyse how the sample geometry affect the material response;

- to analyse if delamination affect the cohesive failure;

- to investigate if digital volume correlation can be used to analyse paperboard;

- to observe how paperboard deforms as well as how the internal structure evolves during tensile loading;

CHAPTER 2

Theoretical background

In this chapter, the behaviour of paperboard when subjected to tensile loading is described. The concept of widening is explained and the corresponding mathematical definition is derived. Furthermore, delamination and relaxation are explained and the impact of sample length, strain rate and moisture content on the response of paperboard during tensile loading is discussed. At the end of the chapter, the method of x-ray tomography as well as the imaging analysis technique, digital volume correlation, are also explained.

2.1 Material properties

2.1.1 Response of paperboard under tensile loading

Figure 2.1 shows stress-displacement curves for tensile experiments on paperboard strips with different lengths. In this figure it can be seen that the post-peak behaviour relates to the length of the sample. This is a known phenomenon that has been investigated in previous studies [3]. Note that length is in this entire report defined as the length between the clamps in the tensile testers, where the paperboard strips are secured, when experiments are performed.

In Figure 2.1 it can be seen that the short sample shows a stable descending stress-displacement curve after failure while the longer sample has a sudden drop in load when failure strength is reached. How a sample behaves after failure is directly related to the amount of elastic energy stored in the sample at failure strength. If the elastic energy is greater than the fracture energy, the load will drop in a rupture-like manner. A stable descending stress-displacement curve is due to that the available elastic energy is always less than the energy needed to cause complete failure. The stable

post-peak behaviour is referred to as the cohesive behaviour and is characterised by a relation between the widening of the localised failure zone and descending load. After failure strength is reached, the localised failure zone widens while elastic relaxation occurs in the rest of the sample.
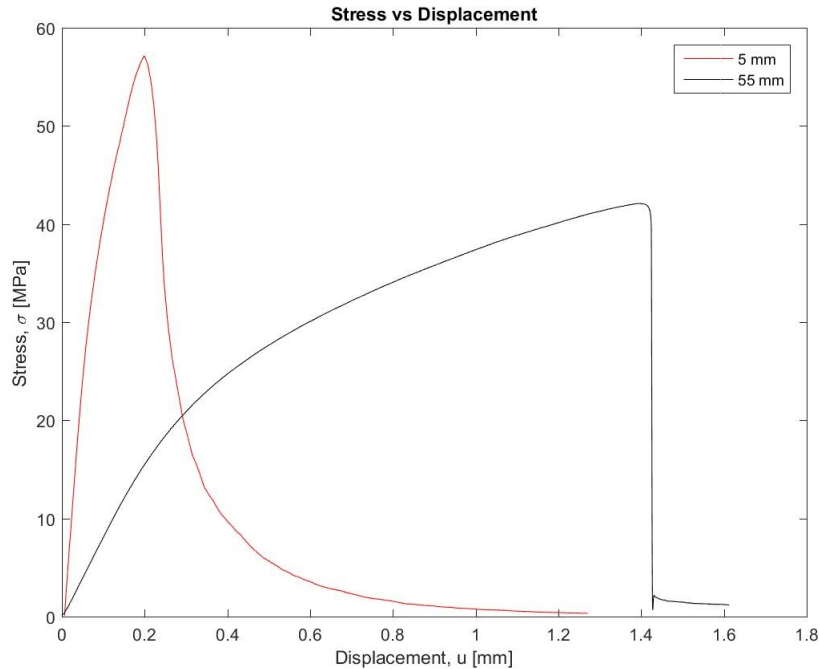
Figure 2.1: Stress-displacement curves from tensile experiments performed on paperboard strips with different lengths.

A stress-displacement curve obtained from a tensile test with a paperboard strip length that results in a stable descending part can be divided into the following regions:

- linear behaviour;

- hardening;

- cohesive behaviour.

For the first part of a stress-strain curve Hooke's law of elasticity can be applied and the slope is equal to the Young's modulus. When the yield stress is reached the characteristics of the curve changes. The increase in stress is no longer linear to the increase in strain. The part between yield stress and failure strength, where the increase in stress is non-linear to the increase in strain, is called the hardening part of the curve.

When the failure strength is reached, localisation of the damage with further loading leads to complete failure. After the failure strength the stress decreases as the deformation increases, this is the cohesive part of the curve. At the end of the curve the sample will be separated at the point of final failure.

2.1.2 Strain energy density

From Figure 2.2 it is clear that the strain energy density is the area under the stress-strain curve, limited by the strain at failure. The strain at this point is called the failure strain and is denoted ϵ_f. Mathematically, the strain energy density W is therefore defined as,

$$W = \int_0^{\epsilon_f} \sigma(\epsilon)d\epsilon. \tag{2.1}$$

The strain energy density can be divided into an elastic and a plastic part according to Figure 2.2, where W_e stands for elastic strain energy density and W_i stands for inelastic strain energy density. The difference between W_e and W_i is that W_e returns back to the material when unloading, while W_i leads to permanent changes in the fibre network. The strain energy density can then be expressed in the following way [3],

$$W = W_e + W_i. \tag{2.2}$$
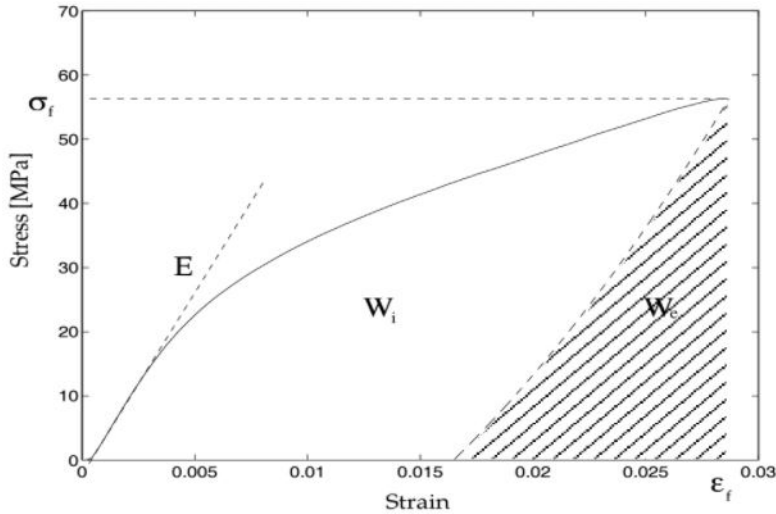
Figure 2.2: Strain energy density divided into one elastic part and one plastic part. The dotted line, dividing W_i and W_e, corresponds to if the sample is unloaded right before failure, picture taken from [3].

With the assumption that the unloading follows the same slope as the Young's modulus seen in Figure 2.2 the uniform unloading strain during failure can be described as [11],

$$\epsilon' = \epsilon_f - \frac{\sigma_f - \sigma}{E}. \tag{2.3}$$

2.1.3 Fracture energy

The stored elastic energy for the longer specimen in Figure 2.1 is higher than the required energy for complete failure and hence the specimen breaks immediately. This

is not the case for the shorter specimen, and, as can be seen in Figure 2.1, it has to be further elongated after σ_f to break. The reason for the change in failure characteristics is that longer samples experience a larger displacement before failure strength, which means that more elastic energy is stored in the specimen before the failure strength is reached. To describe the fracture energy G_f, the widening of the localised zone, w, is derived, cf. Figure 2.3.
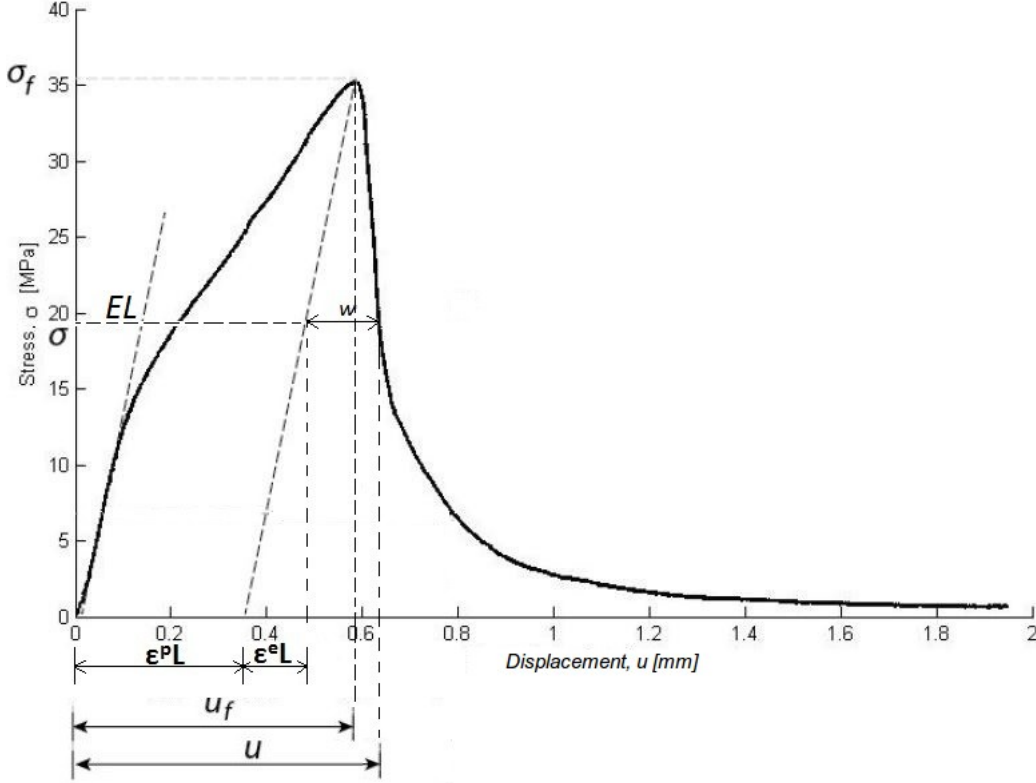
Figure 2.3: Stress-displacement curve for tensile loading of a 5 mm long test specimen of paperboard.

In Figure 2.3 certain parameters are defined; E is the Young's modulus, L is the length of the undeformed specimen and u_f is the displacement of the test specimen at σ_f. The displacement and stress u and σ respectively are points on the curve. Furthermore, $\epsilon^p L$ and $\epsilon^e L$ are the plastic and elastic elongation, respectively. From Figure 2.3 it can be seen that the widening is defined as,

$$w(\sigma) = u(\sigma) - (\epsilon^p + \epsilon^e(\sigma))L = u - \epsilon' L. \tag{2.4}$$

Note that when widening occurs the failure strength has been reached, resulting in a plastic strain that is constant, i.e. not depending on the stress. Equation (2.4) may then be rewritten using Eq. (2.3) as,

$$w(\sigma) = u - u_f + \frac{\sigma_f - \sigma}{E}L. \tag{2.5}$$

10

In Figure 2.4, the concept of widening is graphically shown and further explained. The graph in this figure should be thought of as experimentally obtained, but is simplified with the assumption of no plasticity.
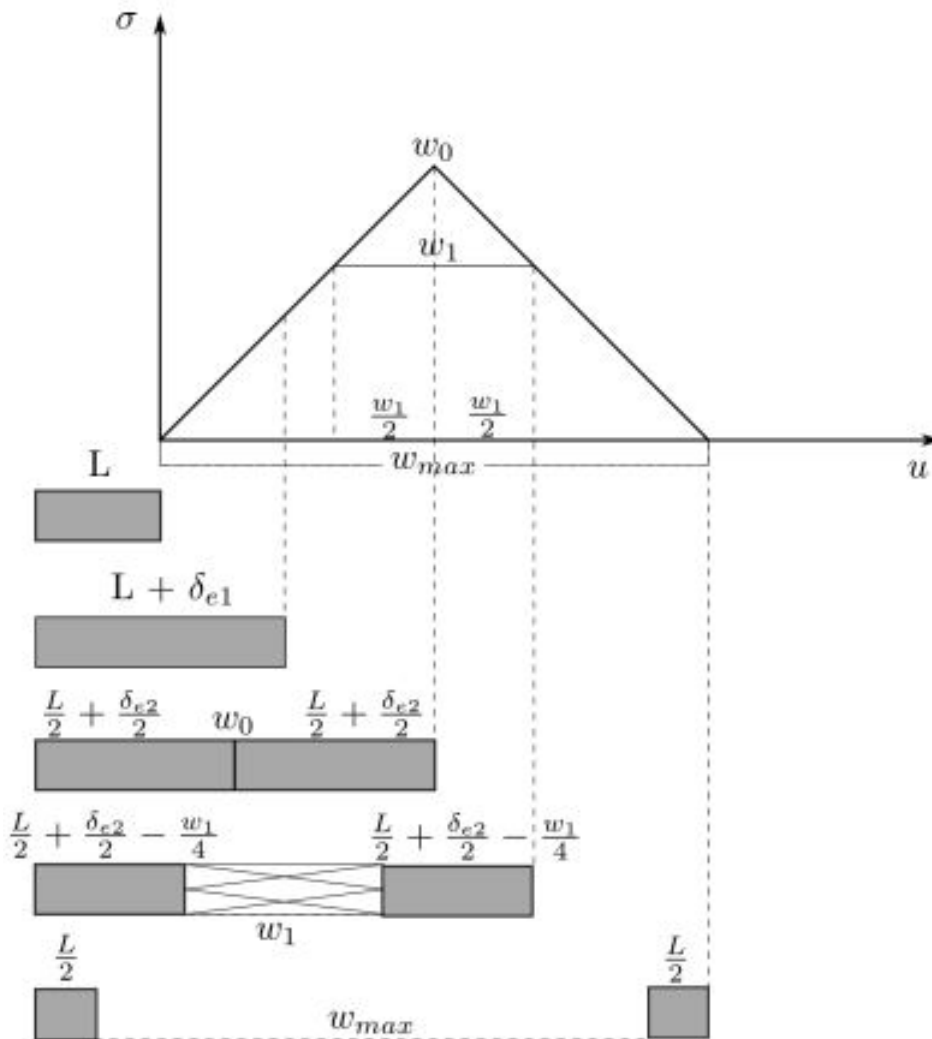
Figure 2.4: A schematic explanation of the concept of cohesive widening, with the simplification of no plasticity, picture taken from [11].

At the beginning of an experiment, a paper strip of length L is secured in the tensile tester. It is then elastically elongated until it reaches the point w_0. At this point, the localised failure zone will initialise and so will the widening. Hence, the widening at this point is equal to $w = 0$. At this point the paper strip may be divided into two parts, for simplification assume that each part have the length $L/2 + \delta_{e2}/2$ where δ_{e2} corresponds to the maximum elastic elongation of the original paper strip. When further elongated, the widening increases and becomes $w = w_1$. The increase in widening results in a total relaxation of $w_1/2$ due to the form of the graph. This corresponds to a relaxation of $w_1/4$ in each of the two paper strip parts. When the maximum widening is reached, the paper strip will completely break into two parts. Due to the simplification that no plasticity exists, the length of the two parts will be

11

$L/2$ [11].

From the data in Figure 2.2 and (2.5) the relationship between cohesive stress and widening is obtained and may be seen in Figure 2.5. $N_{\max}$ corresponds to the maximum slope of the cohesive stress-widening curve and is defined as,

$$N_{\max} = -\left.\frac{d\sigma}{dw}\right|_{\max}.$$

(2.6)
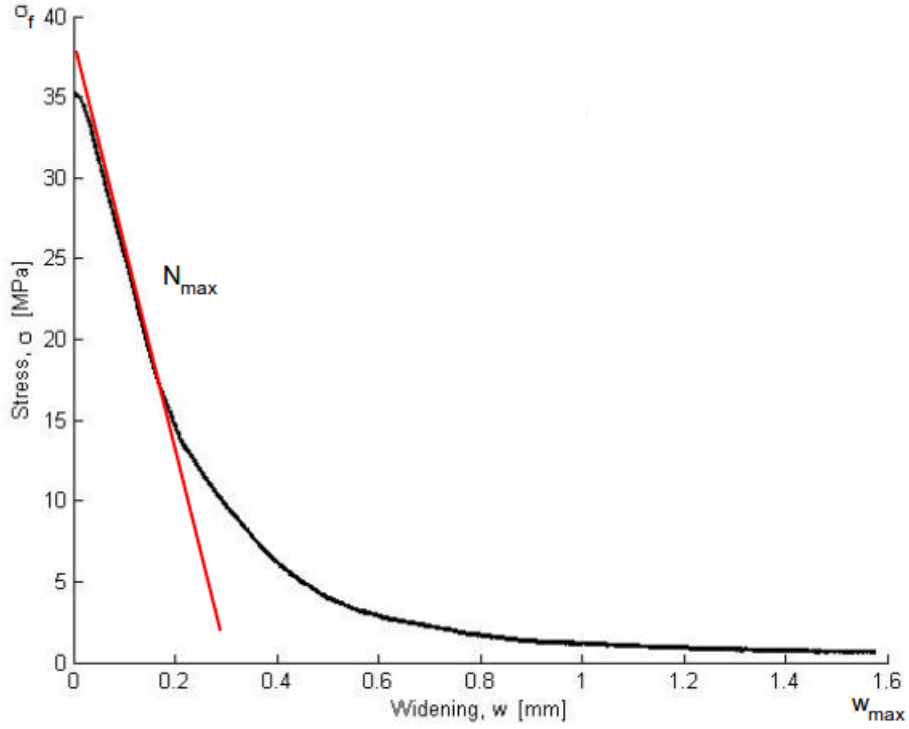
Figure 2.5: Cohesive stress-widening curve from a tensile test on paperboard, picture taken from [1].

The area under the graph of the cohesive stress-widening curve is defined as the fracture energy G_f:

$$G_f = \int_0^{w_{\max}} \sigma(w)dw = \sigma_f \int_0^{w_{\max}} \frac{\sigma(w)}{\sigma_f}dw,$$

(2.7)

where $w_{\max}$ is the widening at which $\sigma = 0$. To link $N_{\max}$ and G_f the length measure w_N,

$$w_N = \frac{\sigma_f}{N_{\max}},$$

(2.8)

and the dimensionless parameters y, x and $x_{\max}$ are introduced,

$$y = \frac{\sigma(w)}{\sigma_f},$$
$$x = \frac{w}{w_N}, \tag{2.9}$$
$$x_{\max} = \frac{w_{\max}}{w_N}.$$

Using the definitions in Eq. (2.8) and Eq. (2.9) in Eq. (2.7) gives

$$G_f = \sigma_f w_N \int_0^{x_{\max}} y(x)dx = \sigma_f w_N g, \quad \text{where} \quad g = \int_0^{x_{\max}} y(x)dx. \tag{2.10}$$

Rewriting Eq. (2.10) gives that a length measure defined by the ratio of the fracture energy and failure strength is obtained as,

$$w_G = g w_N, \quad \text{where} \quad w_G = \frac{G_f}{\sigma_f}. \tag{2.11}$$

Relations between stress and widening are usually on the form

$$\frac{\sigma}{\sigma_f} = f_G\left(\frac{w}{w_G}\right), \tag{2.12}$$

where, f_G is a continuously or piece-wise differentiable monotonic decreasing function [12]. The stress has been normalised by the failure strength and the widening has been normalised by the length measure w_G. An alternative is to relate stress and widening as,

$$\frac{\sigma}{\sigma_f} = f_N\left(\frac{w}{w_N}\right), \tag{2.13}$$

where, f_N is also a continuously or piece-wise differentiable monotonic decreasing function, the stress has been normalised in the same way as in Eq. (2.12), but the widening has been normalised by the length measure w_N.

Tryding and Ristinmaa (2017) proposed a cohesive law as [12],

$$\frac{\sigma}{\sigma_f} = f\left(\left(\frac{w}{w_N x_c}\right)^{\frac{1}{c}}\right), \tag{2.14}$$

where c and x_c are two constants. It was shown in [12] that if Eq. (2.14) is a continuously decreasing function with slope $N(w)$ then the two constants c and x_c are uniquely dependent on each other. This means that the value of x_c only depends on the constant c, $x_c = x_c(c)$. Hence, c can be seen as a shape parameter, characterising the shape of the normalised cohesive stress-widening curve and x_c is a function, depending on the choice of the explicit function in Eq. (2.14).

An example of a normalised cohesive stress-widening curve can be seen in Figure 2.6, where the normalised stress is on the y-axis and the normalised widening is on the x-axis.
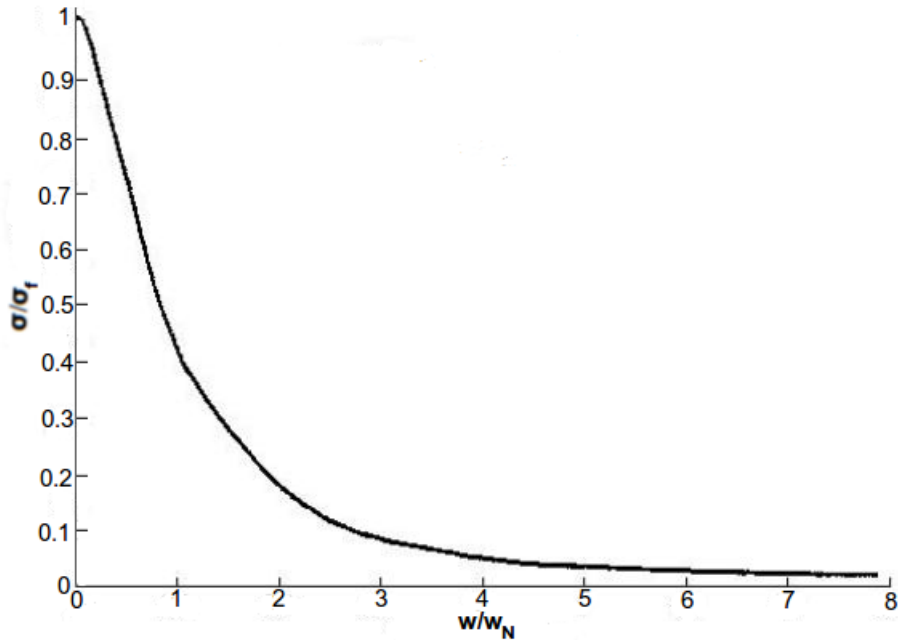
Figure 2.6: A normalised cohesive stress-widening curve for a tensile test on paperboard.

2.1.4 Sample length

The post-peak behaviour is related to the sample length, which is seen in Figure 2.1. The shorter sample in Figure 2.1 has a length below L_{stable}, which is defined as the longest sample length that results in a stable post-peak curve, while the longer sample in Figure 2.1 has a length above L_{stable}. If the length is above L_{stable} an immediate drop of load occurs on the descending part of the curve. When it is an immediate drop of load it almost always occurs directly after failure strength is reached [3]. Furthermore, if the load drops from a point of instability to zero load, the post-peak behaviour is said to be unstable. The shortest length for an unstable post-peak behaviour is defined as $L_{critical}$. Note that the load may drop from a point of instability to a load that is larger than zero. This occurs when $L_{stable} < L < L_{critical}$ [3]. A sample with a length within this interval has a post-peak behaviour that is said to be semi-stable.

The longest sample length for a stable descending post-peak curve, L_{stable} can be derived starting from Eq. (2.4) as,

$$u = (\epsilon_e(\sigma) + \epsilon_p)L + w(\sigma). \tag{2.15}$$

If instability occurs then it will yield that the change of elongation is zero at the same time as the change in load is less than zero. Since $\epsilon_p = constant$ an incremental change of Eq. (2.15) leads to

14

$$\delta u = \frac{\partial \epsilon_e(\sigma) L}{\partial T} \delta T + \frac{\partial w(\sigma)}{\partial T} \delta T = 0. \tag{2.16}$$

Where $T = \sigma A_0$, and $\delta T = \delta \sigma A_0$, and A_0 is the cross-sectional area at the failure load that is assumed to be constant during the cohesive failure. Hence, Eq. (2.16) can be rewritten as,

$$(\frac{\partial \epsilon_e(\sigma)}{\partial \sigma} L + \frac{\partial w(\sigma)}{\partial \sigma}) \delta \sigma = 0. \tag{2.17}$$

Furthermore, $\delta \sigma < 0$, due to the decrease in load and that $A_0 > 0$. This results in that the part of Eq. (2.17) within the brackets has to be equal to zero,

$$\frac{\partial \epsilon_e(\sigma)}{\partial \sigma} L + \frac{\partial w(\sigma)}{\partial \sigma} = 0. \tag{2.18}$$

Since the unloading part of the graph at failure in Figure 2.3 is assumed to be linear, then,

$$\delta \sigma = \frac{\partial \sigma}{\partial \epsilon_e} \delta \epsilon_e = E \delta \epsilon_e \Rightarrow \frac{\partial \epsilon_e}{\partial \sigma} = \frac{1}{E}. \tag{2.19}$$

By inserting Eq. (2.19) in Eq. (2.18) the following expression can be obtained,

$$\frac{1}{E} L + \frac{\partial w(\sigma)}{\partial \sigma} = 0. \tag{2.20}$$

From Figure 2.5 the following relation holds,

$$\delta \sigma = \frac{\partial \sigma}{\partial w} \delta w = -N(w) \delta w \Rightarrow \frac{\partial w}{\partial \sigma} = -\frac{1}{N(w)}, \qquad 0 < w < w_{max}. \tag{2.21}$$

Inserting Eq. (2.21) into Eq. (2.20) results in the following expression,

$$\frac{1}{E} L - \frac{1}{N(w)} = 0 \Rightarrow L = \frac{E}{N(w)}. \tag{2.22}$$

From Eq. (2.22) the lowest value of L is when the slope is maximum i.e. at N_{max}. The criterion for the length of the sample if a stable post-peak curve is desired is therefore defined as,

$$L_{stable} = \frac{E}{N_{max}}. \tag{2.23}$$

To define $L_{critical}$, Figure 2.2 has to be analysed again. Assuming plane stress conditions, the strain energy density for the sample in Figure 2.2 that has a sudden drop of stress can be expressed as,

$$W_e = \frac{1}{2} \frac{\sigma_f^2}{E}. \tag{2.24}$$

If L is now defined as the sample length of a specimen that has an immediate drop of load to zero, then Eq. (2.25) yields

15

$$W_e L > G_f. \tag{2.25}$$

This means that the stored energy in the sample is enough to get complete failure immediately after the point of instability. Equation (2.25) can then be rewritten as,

$$L > \frac{G_f}{W_e}. \tag{2.26}$$

By combining this with Eq. (2.24), Eq. (2.27) yields

$$L > \frac{2EG_f}{\sigma_f^2}. \tag{2.27}$$

Multiply E/σ_f on both sides of Eq. (2.11) results in,

$$\frac{EG_f}{\sigma_f^2} = g\frac{E}{N_{\max}}. \tag{2.28}$$

By using Eq. (2.27) together with Eq. (2.28), the following holds

$$L > \frac{2gE}{N_{\max}}. \tag{2.29}$$

From the definition of L_{stable} in Eq. (2.23), Eq. (2.29) can be written as,

$$L > 2gL_{stable}. \tag{2.30}$$

Since L was defined as a sample length with immediate drop of load to zero, this also means that the shortest sample length that causes an immediate drop of load to zero is defined as,

$$L = 2gL_{stable} = L_{critical}. \tag{2.31}$$

This further means that if a sample has a drop of load to a value other than zero the length of the sample will be in the interval

$$L_{stable} < L < L_{critical}. \tag{2.32}$$

Using Eq. (2.31) this can then be expressed as,

$$L_{stable} < L < 2gL_{stable}. \tag{2.33}$$

2.1.5   Size effects

When analysing the in-plane behaviour of a material, it is of importance to take sample size effects into account. Hagman and Nygårds (2012) analysed how results from tensile tests on paperboard depend on the length to width ratio. It was shown that the form of the stress-displacement curve depends on the sample size. Yield stress, amount of hardening and failure strain all changed when the length to width ratio was changed. Wider specimens exhibit a larger number of localised strain zones. This

is due to that the probability that a zone with higher strain immediately crosses the whole specimen is lower. Hence, the other parts may elongate further, leading to a higher strain at break [13].

Hagman and Nygårds (2012) changed both the sample width and length to be able to analyse the size effects. This was also done to determine how similar the global and local properties of the material are. It was shown that the results from a sample tested with standard size differed compared to when the size was changed to investigate the local properties. Standard size was in their case referred to as length 100 mm, width 15 mm and a rate of displacement of 100 mm/min [13]. If local properties are also analysed it is possible to get a better understanding of how strong the paperboard is at different places. This might in the end be useful when trying to develop a stronger package.

The two curves in Figure 2.1 make it clear that the size of the specimen has an impact on the macroscopically observed behaviour. Theoretically the specimens should break at the same stress regardless of the sample length. This means that the failure strain should differ, but not the failure strength. However, this might not always be the case. It can be seen from Figure 2.1 that a longer test specimen breaks at a lower stress. This is due to the weakest link behaviour, which in principle states that a sample is as strong as it weakest link [3] [14]. This means that for a longer sample there is an increased risk that there are defects that lower the strength of the material. This phenomenon is known, and has been more thoroughly investigated by Moreton in 1968 on carbon fibre [15].

Regarding the different sizes of the paperboard strip used in tensile testing, it should be noted that, if the length is chosen too small, one fibre can stretch all the way from the top clamp to the bottom clamp, which may affect the results. The length of the fibres in paperboard is normally less than 3.6 mm [6] and the length of the paperboard strip should therefore not be lower than this value [3].

Since the way a cohesive stress-widening curve looks depends on the sample size, it might be hard to compare cohesive stress-widening curves for samples with different sizes. If this is desired, the stress-widening curves may be normalised. Tryding and Ristinmaa (2017) showed that for semi-brittle materials, such as cement and paperboard, the normalised cohesive stress-widening curve has the same form, independent of the sample size [12].

2.1.6 Moisture content and strain rate

When paperboard is exposed to water its properties are changed. This means that paperboard is sensitive to the relative humidity of its surroundings [16]. If the relative humidity is increased the paperboard will absorb water, which means that the moisture content of the paperboard increases. Mark et al. (2002) mention that an increase in moisture content in paperboard will result in a decrease in stiffness [17].

This decrease in stiffness can in many cases be undesirable and therefore the relative humidity is an important factor when performing experiments and analyses of paperboard.

The sensitivity to humidity also means that cohesive stress-widening curves of paperboards that have been tested at different relative humidities will not look the same. To still be able to compare the behaviour of the material, the curves can be normalised as was shown by Tryding and Ristinmaa (2017) [12]. This further means that the normalised curve is independent of the moisture content and the cohesive law in Eq. (2.14) is invariant to the moisture content. This also means that the shape parameter c is invariant to the moisture content. Hence, performing experiments on the cohesive behaviour of out-of-plane loaded paperboard at different moisture contents does not influence the shape parameter, c [12].

Gabrielsson, Granlöf and Trost (2017) performed in-plane uniaxial tensile tests on paperboards with different strain rates and moisture contents. They found that the shape parameter c does not depend on the moisture content in the paperboard. It was also found that the strain rate did not influence the shape parameter c [18]. This means that experiments done with different moisture contents and strain rates can be compared, simply by normalising the cohesive stress-widening curves.

2.1.7   Delamination

Gabrielsson (2017) performed short-span tensile tests on different paperboards and came to the conclusion that a thickness increase occurred either before or right after a failure zone was visible in the thickness direction. The point for when a thickness increase was visible differed between different experiments on the same material. The results from Gabrielsson's experiments can be seen in Figure 2.7. As can be seen in this figure, the increase in thickness is first visible at the sample edge after the failure strength is reached. It can also be seen that the point where the thickness increase was visible differed between the samples. The thickness was observed using a high speed camera and an extension microscope [19].
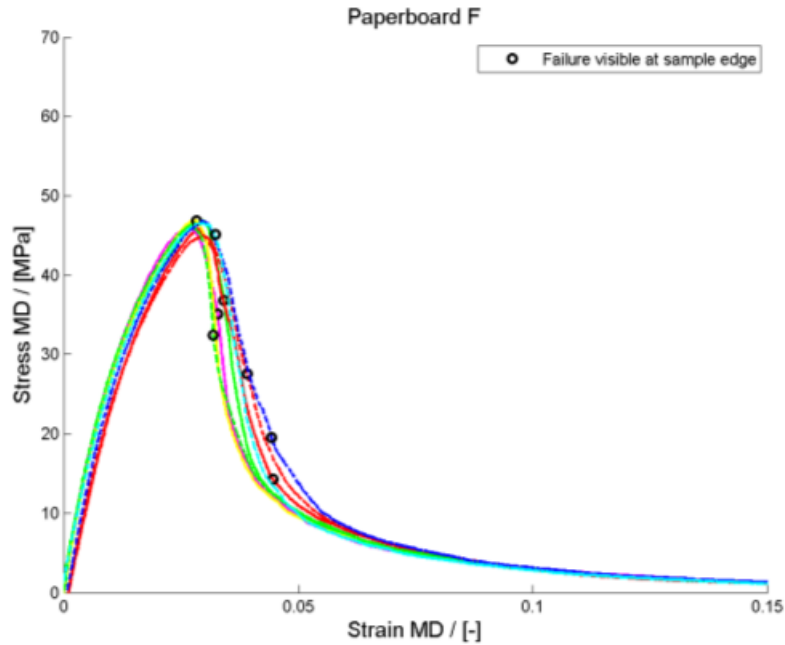
Figure 2.7: The coloured curves are results from tensile experiments performed on paperboard. The black points show when a thickness increase was visible, figure taken from [19].

When paperboard is subjected to loading the internal structure can change, leading to separation of the fibres. This separation of fibres leads to spaces in the paperboard where there are no fibres. This is referred to as delamination [7]. Delamination can be seen in the sample in Figure 2.8. From the figure, it can also be seen that delamination results in a thickness increase.
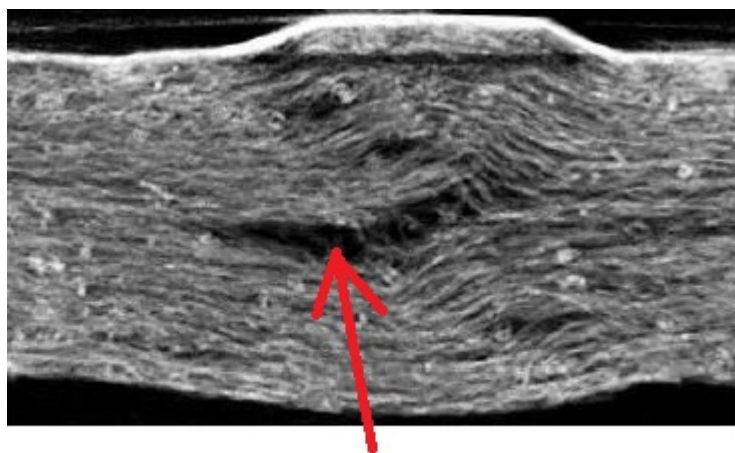
Figure 2.8: The principle of delamination in paperboard, picture taken from [7].

2.1.8 Relaxation

To obtain a three-dimensional image by x-ray tomography takes some time, which means that it is not possible to continuously elongate the specimen in the tomograph during the acquisition time. Therefore certain interesting points along the stress-displacement curve have to be chosen at which the displacement has to be held constant during the time the tomograph acquires the images of the sample. It is important that the material is as still as possible during this time, since movement will affect the result. However, with the displacement held constant under load, relaxation will occur.

The principle of relaxation when performing tensile tests is that the force will decrease even though the displacement is held constant. The reason for this is that the material always strives for equilibrium. Relaxation for creasing of paperboard has previously been investigated with the result that the stress relaxation rate decreases in a logarithmic manner as the displacement is held constant [20]. A typical stress-time curve that describes relaxation can be seen in Figure 2.9.
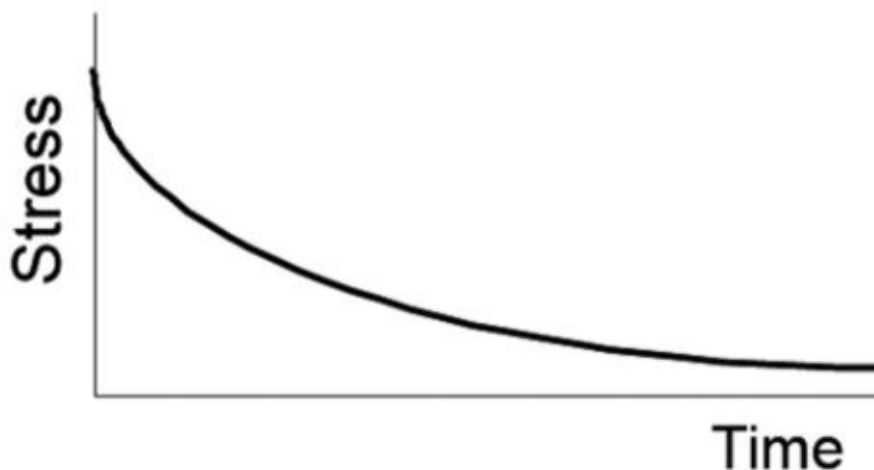
Figure 2.9: A typical stress-time curve that describes relaxation, figure taken from [21].

2.2 X-ray tomography and analysis

2.2.1 X-ray tomography

As described in the introduction, x-ray tomography is a measuring method used for analysis of the inside of a material. In experimental mechanics, x-ray tomography is usually performed using a synchrotron or laboratory x-ray source. One difference between the two sources is the geometry of the x-ray beams. In a synchrotron, parallel beams are produced, while in a laboratory x-ray tomograph, an x-ray tube is used that produce cone beams [10], cf. Figure 2.10. When parallel beams are used, the

resolution is mainly defined by the x-ray detector while when an x-ray tube is used, the cone beam geometry has to be accounted for to define the resolution. The difference in beams also results in that the sample usually has to be rotated 360° when using an x-ray tube, while only 180° are needed if the material is analysed using a synchrotron [10].
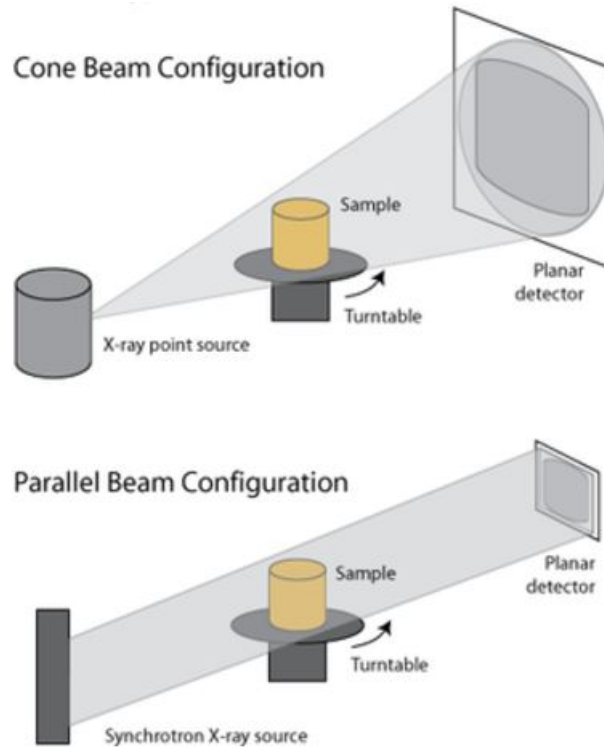
Figure 2.10: Cone-formed beam from an x-ray tube at the top and parallel beam from a synchrotron at the bottom, picture taken from [22].

One of the main advantages with synchrotron radiation is that it allows much higher photon flux compared to an x-ray tube, resulting in shorter scanning times [10] [23]. Furthermore, monochromatic x-rays are often used in a synchrotron while polychromatic x-rays are used in a laboratory [23]. Due to the fact that the x-rays are polychromatic in a laboratory x-ray tomograph this will lead to something called beam hardening. Beam hardening means that soft x-rays, which are x-rays with low energy, are stopped when entering a specimen. This is an artefact that does not occur in a synchrotron if monochromatic x-rays are used. Although it is possible to filter out the soft x-rays in a laboratory tomograph, this leads to an even lower flux, which results in longer scanning times [10].

Although a synchrotron is often the best way to get a high resolution three dimensional image of the material in a relative short time, there are some advantages using a laboratory x-ray tomograph instead. These are mainly the high cost effectiveness, user friendliness and accessibility [23]. For these reasons, a laboratory tomograph may in many cases be a good choice when analysing materials.

To be able to reconstruct a three dimensional image from acquired radiographs the difference in intensity with and without the sample mounted has to be measured. For a laboratory x-ray tomograph this is done for multiple angles usually between 0-360°, which, in the end, can be reconstructed into a three dimensional image of the sample.

The tomograph reconstruction from the generated radiographs can mainly be done in two different ways, using an algebraic method or an analytic method. The principle of the algebraic method is that a system of equations is solved by a computer, with the attenuation coefficient for each voxel (which is a small sub-volume) as unknown. The analytic method uses a Fourier transform to backproject the transmitted intensity and from this determine the attenuation coefficient for each voxel. Since the sample is not sampled uniformly due to the fact that it rotates around one axis, the back projection has to be filtered. The analytic method is, for this reason, also called filtered back projection reconstruction [10].

To show how the attenuation coefficient and the intensity that is measured is related, Beer-Lambert's law is given as,

$$I_x = \int I_0(E) e^{\sum_i (-\mu_i(E)x_i)} dE. \tag{2.34}$$

In Eq. (2.34) I_x is the intensity after the sample at a distance x from the x-ray source, I_0 is the intensity of the beam before the sample, μ is the linear attenuation coefficient and E is the x-ray energy. For a polychromatic source it has to be taken into account that the attenuation coefficient depends on the x-ray energy [22]. If a synchrotron source is used instead, which produces monochromatic beams, Eq. (2.34) can be simplified since the energy is constant, resulting in [22],

$$I_x = I_0 e^{\sum_i (-\mu_i x_i)}. \tag{2.35}$$

2.2.2 Image analysis

When experiments that result in images have been performed, the images need to be analysed to extract valuable information. Depending on the objective of the analysis, there are several different methods to do this. When the deformation of an object is of interest, digital image correlation (DIC) and digital volume correlation (DVC) may be suitable. By using DIC or DVC it is possible to follow small areas or volumes in the material during deformation. For DIC it is many small areas at the surface of the material that are followed while for DVC many small three dimensional volumes can be followed during deformation. This means that when using DVC to analyse the response of a sample upon external loading, the structure in the entire volume of the sample needs to be known and not just the surface. Thus, a three dimensional imaging method, such as x-ray tomography, has to be used. This makes it possible to get information about the entire volume of the sample. This is not needed for DIC since only the surface is analysed with this method [24].

The principle when using DVC is the following:

First a three dimensional image of the material is constructed using, e.g. an x-ray tomograph. After this, the sample is subjected to some external perturbation that results in changes in the material structure. When the material has reached a new equilibrium, a new three dimensional image is constructed. Digital volume correlation is then used to compare the two three dimensional images to be able to find how the structure in the material has changed. DVC takes one small volume in the first image, with a certain structure, and then looks through the second image until it finds a volume with the same structure. The structure in the small volumes might change a bit but DVC finds the volume in the new image that has the best correlation with the original image. The assumption is generally that only a small movement and perhaps also structural change occurs in each small volume even if the structure in the entire sample might change a lot. This process is repeated until all small volume pieces from the original image have been found in the new image. It is then possible to see how each small volume has moved due to the external perturbation. From this, displacement fields can be constructed in all three directions. When displacement fields are known it is also possible to calculate strain fields [24].

Digital volume correlation results in displacement fields that includes both rigid body displacement and displacement due to strain in the sample. Rigid body displacement can be of interest to get better understanding of why and how the sample moves during loading, while displacement due to strain in the sample is related to the response of the material.

One shortcoming of the DVC method is the so called stepped displacement field. This has to do with the fact that the images are divided into voxels, and hence the resolution of the calculated displacements is of the size of a voxel. This results in that steps in the displacement calculations are obtained, which also affects the calculated strains. This phenomenon is illustrated in Figure 2.11 for DIC, and the same principle holds for DVC. To resolve this problem sub-voxel refinement may be applied, which smooths the steps. Without the sub-voxel refinement certain artificial patterns in the strain fields might occur [24].
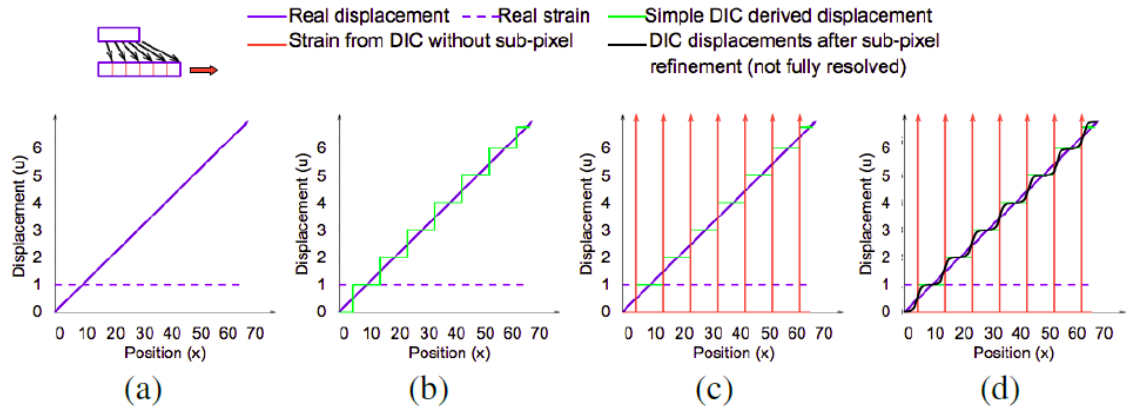
Figure 2.11: Schematic image displaying the shortcomings of sub-pixel resolution for DIC. The principle is the same for DVC and sub-voxel resolution, figure taken from [24]. (a) Real displacement and real strain. (b) Displacement due to integer steps. (c) Strains due to integer displacement steps. (d) Displacement after applying sub-pixel refinement.

Figure 2.11 shows how a given displacement field might be quantified by DIC with and without sub-pixel refinement. Since the same principle holds for DVC and sub-voxel refinement the same figure can be used to describe this. A basic DVC program is only able to determine if a part of the reference image has moved by whole voxels. This results in steps, as shown in Figure 2.11 (b). When calculating the strains from such displacements, these steps will result in that there exists either extremely large strains, or none at all, as may be seen in Figure 2.11 (c). By using sub-voxel refinement, a result more similar to the real displacement may be calculated, as seen in Figure 2.11 (d). Some artefacts may still be present if the sub-voxel displacement are not fully resolved.

2.2.3 Strain calculations

From the calculated displacement fields using DVC, it is possible to calculate the strains within the material using continuum mechanics. In Figure 2.12, a schematic image describing the reference state and the deformed state of a continuum particle is shown.
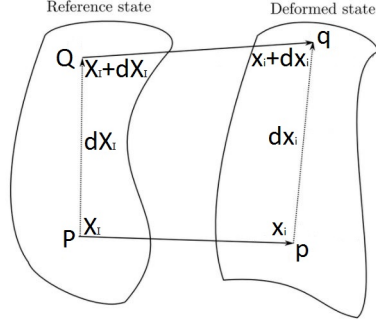
Figure 2.12: A continuum particle in its reference- and deformed state.

In Figure 2.12, P and Q denote points in the reference (undeformed) configuration, X_I denotes the position vector to P, and $X_I + dX_I$ denotes the position vector to Q, where $I = 1, 2, 3$ represents the three orthogonal directions. The points P and Q are assumed to be infinitely close to each other, represented by the distance dX_I. Furthermore, p and q correspond to the points in the reference configuration with an added displacement vector. Thus it is possible to describe the location of point p by using the position vector as,

$$x_i = \delta_{iJ} X_J + u_i(X_J, t), \tag{2.36}$$

where $u_i(X_J, t)$ corresponds to the added displacement vector.

The position vector for point q is,

$$x_i + dx_i = \delta_{iJ} X_J + \delta_{iJ} dX_J + u_i(X_J + dX_J, t), \tag{2.37}$$

where $u_i(X_J + dX_J, t)$ corresponds to the added displacement vector, taken into account that the displacement vector before deformation was $X_J + dX_J$.

The distance between p and q can be written as,

$$dx_i = \delta_{iJ} dX_J + du_i(X_J, t), \text{ where } du_i = u_i(X_J + dX_J, t) - u_i(X_J, t). \tag{2.38}$$

Using that $du_i = (\partial u_i / \partial X_J) dX_J$ in Eq. (2.38) gives,

$$dx_i = (\delta_{iJ} + u_{i,J}) dX_J = F_{iJ} dX_J, \quad \text{where } u_{i,J} = \frac{\partial u_i}{\partial X_J}. \tag{2.39}$$

The distance between the reference points dS and the distance between the points in the deformed state ds are defined as,

$$dS^2 = dX_J dX_J, \quad \text{and} \tag{2.40}$$

$$ds^2 = dx_j dx_j. \tag{2.41}$$

Equation (2.41) may be rewritten using Eq. (2.39) as,

$$ds^2 = (\delta_{iJ} + u_{i,J})(\delta_{iK} + u_{i,K})dX_J dX_K = F_{iJ}F_{iK}dX_J dX_K = C_{JK}dS^2. \qquad (2.42)$$

Hence, the difference, $ds^2 - dS^2$ is given as [11],

$$ds^2 - dS^2 = C_{JK}dS^2 - \delta_{JK}dS^2 = (C_{JK} - \delta_{JK})dS^2, \qquad (2.43)$$

where

$$C_{JK} - \delta_{JK} = u_{J,K} + u_{K,J} + u_{i,J}u_{i,K}. \qquad (2.44)$$

The Green strain tensor E_{JK} is defined as,

$$E_{JK} = \frac{1}{2}(u_{J,K} + u_{K,J} + u_{i,J}u_{i,K})dX_J dX_K = \frac{1}{2}(C_{JK} - \delta_{JK}). \qquad (2.45)$$

Using the Green strain tensor in Eq. (2.43) gives,

$$ds^2 - dS^2 = 2E_{JK}dS^2 = 2dX_J E_{JK}dX_K. \qquad (2.46)$$

The Green strain tensor takes the following form when written on matrix format

$$\boldsymbol{E} = \begin{bmatrix} E_{xx} & E_{xy} & E_{xz} \\ E_{yx} & E_{yy} & E_{yz} \\ E_{zx} & E_{zy} & E_{zz} \end{bmatrix} \qquad (2.47)$$

where E_{xx}, E_{yy} and E_{zz} corresponds to the normal strains and the rest are shear strains.

2.3 Summary

In this chapter it was shown that a longer sample leads to more stored elastic energy in the paperboard before failure strength. If the stored elastic energy is higher than the energy needed for fracture a brittle failure will occur, otherwise widening will occur after failure strength is reached, resulting in a cohesive failure. It was shown that if the cohesive stress-widening curve is normalised the shape of the curve is independent of sample length, strain rate and moisture content.

The concept and benefits of x-ray tomography has been explained as well as the usage of the resulting images. The images may be used to calculate displacement fields using digital volume correlation. From the displacement fields it has been shown how strain fields may be calculated using continuum mechanics.

CHAPTER 3

Experimental method

In this chapter the experiments performed, both at Tetra Pak and at Lund University, are explained. The reasons for the experiments performed at Tetra Pak were to analyse how the sample geometry affect the material response as well as to investigate if delamination can cause in-plane failure. The experiments at Lund University was performed to observe how the paperboard deforms and the internal structure evolves during tensile loading as well as to investigate if digital volume correlation can be used to analyse paperboard.

3.1 Short-span experiments

3.1.1 Short-span tensile tests

To perform short-span tensile tests at Tetra Pak a tensile tester from Instron was used. The tensile tester was displacement controlled and connected to a computer that collected data. To fasten the paperboard, custom made clamps were mounted in the machine. The clamps were constructed as a circular clamp at one side and a straight clamp on the other side, one of the clamps can be seen in Figure 3.1. The clamps were pneumatic controlled and the pressure in the system was set to 3 bars during the experiments. The distance between the clamping points was set to 4 mm, 5 mm and 10 mm for the different experiments. The length was alternated so that size effects could be studied. To be able to analyse size effects also the width was altered. The width was set to 3 mm, 5 mm and 15 mm for the different experiments. A notched sample with notch width of 3 mm was also used since this was the sample geometry later used in the tomograph.

Regarding the test equipment a loading cell of 10 kN was used to measure the force.

The equipment used was desired to have a stiffness greatly exceeding the stiffness of the test specimen, to have a minimum impact on the results. It is assumed that the stiffness of the equipment used is much higher than the stiffness of the paperboard.

Figure 3.1: The upper clamp used in the tensile tester at Tetra Pak.

To program the loading device, and to record the data from the experiments, the Bluehill software from Instron was used. The displacement rate was set to 0.05 mm/s and the data sampling rate was set to 2 ms. The force and displacements were recorded for each test to provide force-displacement curves.

All the test specimens were cut from sheets of paperboard from the same batch. The paperboard used consisted of one ply, and had clay coating on one side. In Figure 3.2 the geometries of the specimens used in the experiments are displayed and in Table 3.1 the different lengths and widths used are tabulated. To cut the samples of width 15 mm a paper cutting board was used, and to cut the rest of the samples a computer controlled robot from Zünd (model M-1200) was used. To cut out the samples using this machine, the geometry wanted was first constructed in Adobe Illustrator since this was the format needed as input. The paperboard that was going to be cut was then taped by hand onto a flat board.
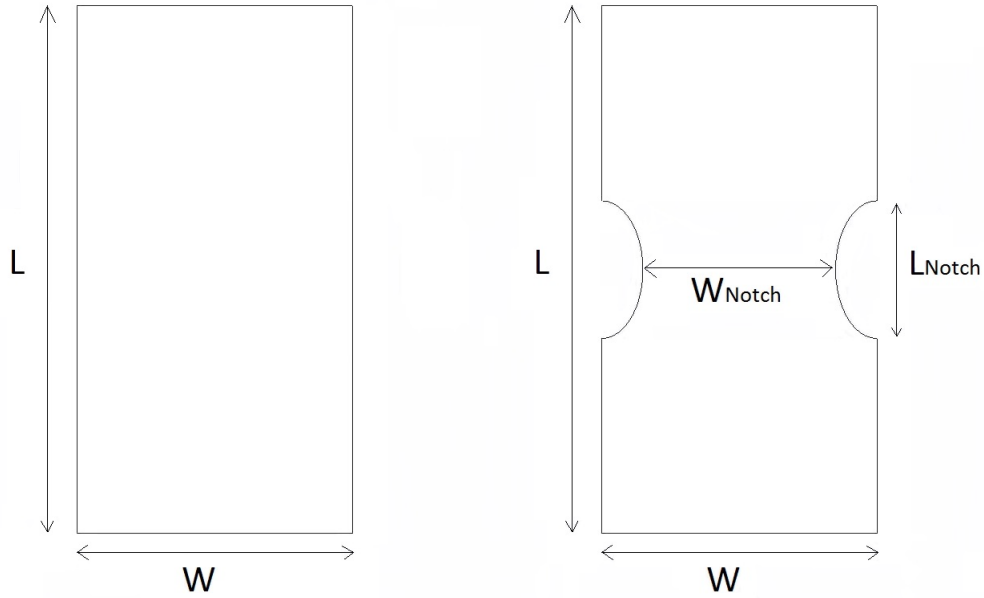
Figure 3.2: Geometries of the paperboard specimens used in the experiments.

Table 3.1: Measurements of the paperboard specimens used in the experiments.

Test Sample	W [mm]	L [mm]	W_{Notch} [mm]	L_{Notch} [mm]
1	3	4	-	-
2	3	10	-	-
3	15	5	-	-
4	15	10	-	-
5	5	10	3	2.5

The paperboard thickness was measured using a L&W Micrometer machine from Lorentzen & Wettre. According to ISO 534 the thickness should be measured three times per sheet on a total of four sheets. In this project the thickness was measured five times per sheet on a total of five sheets. A total mean thickness was calculated according to ISO 534. The thickness was used, together with the forces collected from the tensile tests, to calculate the stresses.

The tensile tests performed at Tetra Pak were performed in a controlled environment. At all times the temperature was set to 23°C and the relative humidity was set to 50 % in accordance with ISO 187. The test specimens were acclimatised by first being put in an oven at 60°C for 30 minutes, and then being in the controlled environment for at least three hours before any experiments were conducted, (in accordance with ISO 187). If any sheet was taken out of the room where the environment was controlled they were acclimatised once again. However, according to ISO 187, test pieces should not be cut before conditioning, this was done for all samples with width different from 15 mm which means that ISO 187 was not followed. The reason not to follow ISO 187 had to do with the fact that the machines needed to cut the other

geometries were located outside of the climate-controlled laboratory.

20 tests were performed in both MD and CD for each length and width combination displayed in Table 3.1. The results were then analysed using a Matlab program where stress-displacement curves first were constructed. From this the Young's modulus for each test could be determined. Using Eq. (2.5) the widening could be calculated and cohesive stress-widening curves constructed. To be able to normalise the cohesive stress-widening curves the length measure w_N was calculated from the experimental data. The cohesive stress-widening curves could then be normalised by dividing the cohesive stress by σ_f and the widening by w_N.

3.1.2   Short-span tensile tests with pre-delaminated samples

To get a better understanding of how delamination affects the strength of a sample, tensile tests with pre-delaminated samples were performed. The pre-delaminated samples were the result of short-span compression tests which were performed using a L&W Compressive Strength Tester STFI machine from Lorentzen & Wettre. Ten shorts-span compression tests were performed in both MD and CD, all samples taken from the same sheet.

The samples were first compressed so that delamination was introduced in the sample, then short-span tensile tests were performed. From this, stress-displacement curves were constructed, which could be compared to the stress-displacement curves for the short-span tensile tests performed with the same size, but without the compression tests. The samples for which both compression and tensile tests were performed, had a length of 5 mm and a width of 15 mm.

3.2   In-situ tensile experiments in the tomograph

The x-ray tomograph used was of the model Xradia520Versa by Zeiss and was located at the 4D Imaging Lab, Division of Solid Mechanics, Lund University. The method it used for reconstruction of the images was filtered back projection, as was described in Section 2.2.1. The in-situ tensile test in the tomograph was performed in an uncontrolled environment. In Figure 3.3 (a) a photo of the tomograph with the different in-situ components is visible.
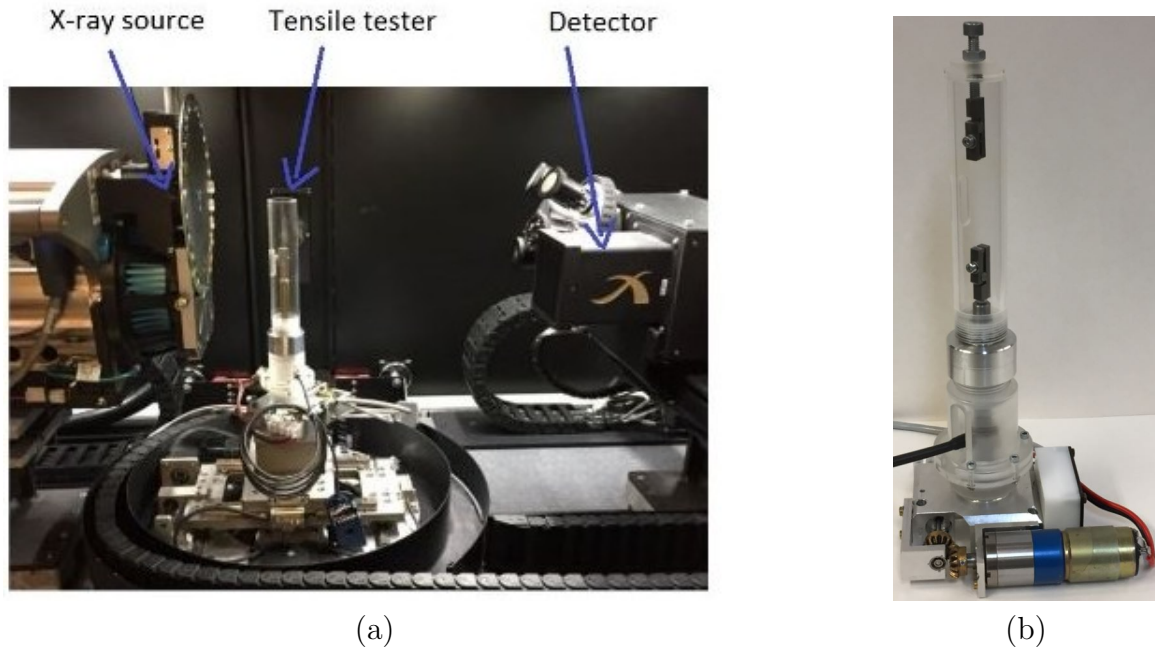
<div align="center">(a)   (b)</div>

Figure 3.3: (a) The tomograph used, with the bottom part of the tensile tester mounted. (b) The tensile tester used in the tomograph.

In Figure 3.3 (a) the x-ray source can be seen to the left, the detector to the right and the bottom part of the mounted tensile tester in the middle.

The tensile testing equipment used in the tomograph, which can be seen in Figure 3.3 (b), differed from the equipment used in the experiments at Tetra Pak. Since the equipment had to be small enough to fit in the tomograph, certain limitations regarding its design existed. The equipment was designed and built at Division of Solid Mechanics, Lund University. It was constructed of two separate pieces, one contained the top clamp and the other contained the bottom clamp together with the rest of the tensile equipment.

The top part of the equipment consisted of the upper clamp, and it was at the top the distance between the grips was adjusted. The grips used were of the same design as for the clamps used in the experiments done in the climate-controlled laboratory at Tetra Pak. In Figure 3.4 the top grip for the tensile tester used in the tomograph is shown. The bottom grip had the same design. The grips were made out of steel with a circular clamp at one side and a straight clamp on the other side. The intention of the design was the same as for the grips used in the laboratory at Tetra Pak, to have a minimal impact on the performed experiment. The clamps were fastened using a screw that was manually tightened using an allen key. By turning a screw and a plastic "roof" the distance between the upper- and the lower grip was adjusted. This was done manually and the distance between the clamps was determined using trial and error until the desired length was reached.
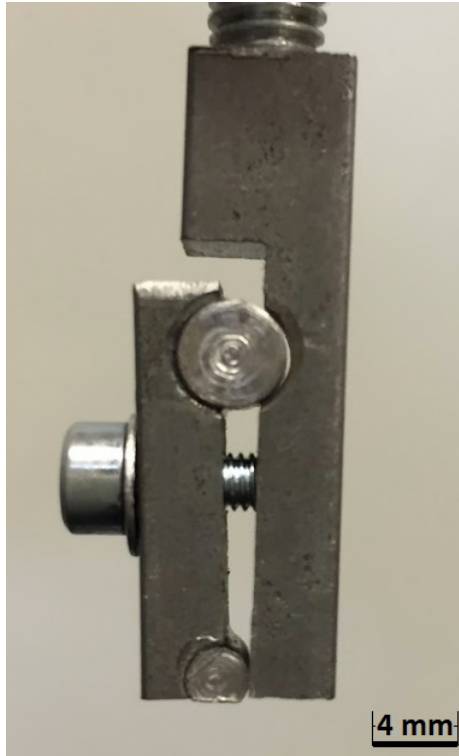
Figure 3.4: The top grip used in the tomograph loading device.

The lower part of the equipment consisted of a cylindrical wall made out of plastic. Inside the wall the bottom grip was located, and it was tightened in the same way as the top grip. The bottom grip was moved using an electric motor, which resulted in displacement of the specimen. The displacement was measured using a strain gauge, and the force acting on the specimen was measured using a load cell of 100 N.

The test specimen was first secured in the top grip, and then lowered down inside the cylindrical wall. It was then secured in the bottom grip and the alignment was done manually. The roof of the plastic pipe was simply laying at the top of the pipe. This was done to get the sample to align a bit by itself. Due to the reason that the roof was not strapped to the rest of the equipment the top part could move a bit sideways when the loading started. This allowed the sample to get more aligned than it would have been if the roof would have been strapped to the rest of the pipe.

The software used in the experiments was custom made for the equipment used. The equipment was displacement controlled using an applied constant voltage. The reason for this had to do with the construction of the equipment. Due to this, the rate of displacement varied with respect to the resistance of the test specimen. With low resistance the displacement rate was high, and with high resistance the displacement rate was low. In this case the voltage was set to 5 V and the sampling rate was set to 10 ms. The points where the displacement was supposed to be held constant was set manually by stopping the machine at certain stresses.

The test specimen used for the experiments in the tomograph was notched, with the dimensions of sample 5 which can be seen in Table 3.1. The reason for the chosen dimensions had to do with the fact that the fibre length normally does not exceed 3.6 mm [6]. It was not desired to have fibres stretching from one clamp to the other, since this perhaps would affect the results [3]. Therefore a shorter length than 3.6 mm was not chosen. Due to the fact that the clamps may affect the failure zone if they are close to it, a length of 10 mm was chosen. The reason for the notches was to force the localisation of the failure zone to propagate at a certain place. This was desired to be able to focus the tomograph at this certain area and know that the failure zone was going to appear there. This made it possible to save time since a smaller area does not take as long time to scan in the tomograph as a larger area for a certain desired resolution. This means that the reason for the notches was simply to get a good resolution of the images from the tomograph. Another advantage due to the chosen geometry was that it was possible to avoid getting the grips in the image. Since they are made out of iron they may interact with the x-rays.

A width of 3 mm was chosen to get a small area to analyse in the tomograph. Even though fibres may stretch along the entire width of the sample this will not affect the results since these fibres are not in contact with the clamps. The reason for the rounded notches had to do with that stress concentrations occurs at sharp edges. The length and width of the notches were chosen by trial and error by performing short-span tensile tests and controlling if the failure zone always localised between the notches. This was the case for samples with the geometry of tests sample 5 in Table 3.1, which is why these measurements were chosen.

3.2.1 Experimental procedure

Regarding the test procedure used in the tomograph, only MD was analysed. A number of six images were taken of the sample on different parts of the stress-displacement curve. This was done by first constructing a reference image, which was taken at load 0 MPa, and then load the sample until a certain amount of stress, where the sample was held at a constant displacement. After relaxation had been taken into account by waiting for 20 minutes a new image was constructed. To find out the time needed between loading stop and tomograph start relaxation experiments were performed, see Appendix A. The amount of displacement between the holding points differed. This was due to the fact that the material changes more rapidly just at the failure strength and therefore small steps between holding points were desired close to that point. The displacement rate between the holding points is shown in Table 3.2 and the settings in the tomograph are shown in Table 3.3.

Table 3.2: Displacement rate between the holding points.

Holding points	Displacement rate [mm/s]
0-1	0.28
1-2	0.20
2-3	0.44
4-5	0.42
5-6	0.49

Table 3.3: Settings used in the tomograph.

Settings	
Power	7 W
Voltage	80 kV
Resolution	3.5 μm
Exposure time	1.5 s
Magnification	4x
Number of projections	1001 projections over 360°

From the relaxation tests, it was found that after approximately 20 minutes the rate of decrease in stress was small enough to start the tomograph. The reason for the 20 minutes wait was simply to get the material closer to the equilibrium state, which results in less movement in the material during the acquisition. If the microstructure of the specimen change too much during the acquisition the obtained images may be unclear and blurry which is undesired.

After the first two images had been constructed the same sample was loaded again from the previous position. It was then loaded to a new stress level and the same procedure was repeated. This was done for six points on the curve, where the reference image was the first point taken at zero displacement. This method was chosen since the displacement between each image was considered small enough to be able to use digital volume correlation between the images.

3.3   Image analysis

Two different methods regarding the analysis of the obtained images from the tomograph were used, one qualitative- and one quantitative method. To visually analyse the obtained images an open source program named Fiji was used [25]. The output from the tomograph was a number of two dimensional images, together making up a volume of the specimen. Fiji made it possible to alter colours and contrasts to get more clear images, as well as reconstruct the three dimensional volume from the two dimensional images. Fiji was also used to measure the thickness of the sample. This was done by calculating the mean intensity of the projection along each line of voxels in the CD-direction, and then, by using a built in measuring tool, it was possible to

quantify the thickness at each holding point.

To analyse the images quantitatively strain fields were constructed using digital volume correlation. A DVC-program named TomoWarp2 [26] was used which resulted in displacement and strain fields. In this program a few parameters were needed as input. The correlation window, the search window and the node spacing had to be chosen. The node spacing corresponds to the distance in pixels between the centre of the voxels analysed, the correlation window corresponds to the size in pixels of the surroundings of the node that is tried to be found after deformation, and the search window corresponds to the region of pixels where the correlation window is searched for. The node spacing and the correlation window were chosen using trial and error while the search window was chosen by first doing a coarse mesh to be able to see the approximative displacements in all directions. From this the required search window could be determined and a finer mesh could be used. The settings regarding search window, correlation window and node spacing used are tabulated in Table B1 in Appendix B.

Between holding points 1-4 the sub-voxel refinement-method called *correlation coefficient* was used with its standard settings. This method is faster compared to more refined methods, but results in lower sub-voxel resolution. Since the deformation was relatively small between the holding points before failure, this method was sufficient. Between holding points 4 and 5 the method *image interpolator translation* was used, with the setting *map coordinates of interpolation order 2* as parameter. This method results in higher sub-voxel resolution, but takes more time. Since failure occurred between holding points 4 and 5 this method was necessary. For further information regarding the settings in TomoWarp2, see [26].

TomoWarp2 was used to analyse the displacements between the tomographic images acquired at consecutive holding points, resulting in three displacement fields between each holding point. These three displacement fields corresponded to the displacements along each of the three coordinate axes. From the displacement fields the DVC program also calculated strain fields.

The normal strains as well as all shear strains were output from the program. To analyse the strain fields Fiji was used, which made it possible to analyse the sample in three dimensions as well as analyse different slices through the volume.

CHAPTER 4

Experimental Results

In this chapter the results from the experiments are displayed. Interesting findings are commented upon and connected to previous research.

4.1   Short-span tensile tests

The short-span tensile tests resulted in force-displacement curves for samples of different lengths and widths. To construct stress-displacement curves, an average thickness of 408 μm of the specimens was measured and used in the calculations. These curves were then reconstructed to cohesive stress-widening curves that were normalised, resulting in normalised cohesive stress-widening curves.

4.1.1   Stress-displacement curves

In Figure 4.1 the stress-displacement curves from the short-span tensile tests performed on specimens of different sizes and geometries are shown. Experiments both for the machine direction and for the cross machine direction are displayed. Note that the stresses shown in the graphs are the First Piola-Kirchhoff stresses due to the fact that the original cross sectional area was used.
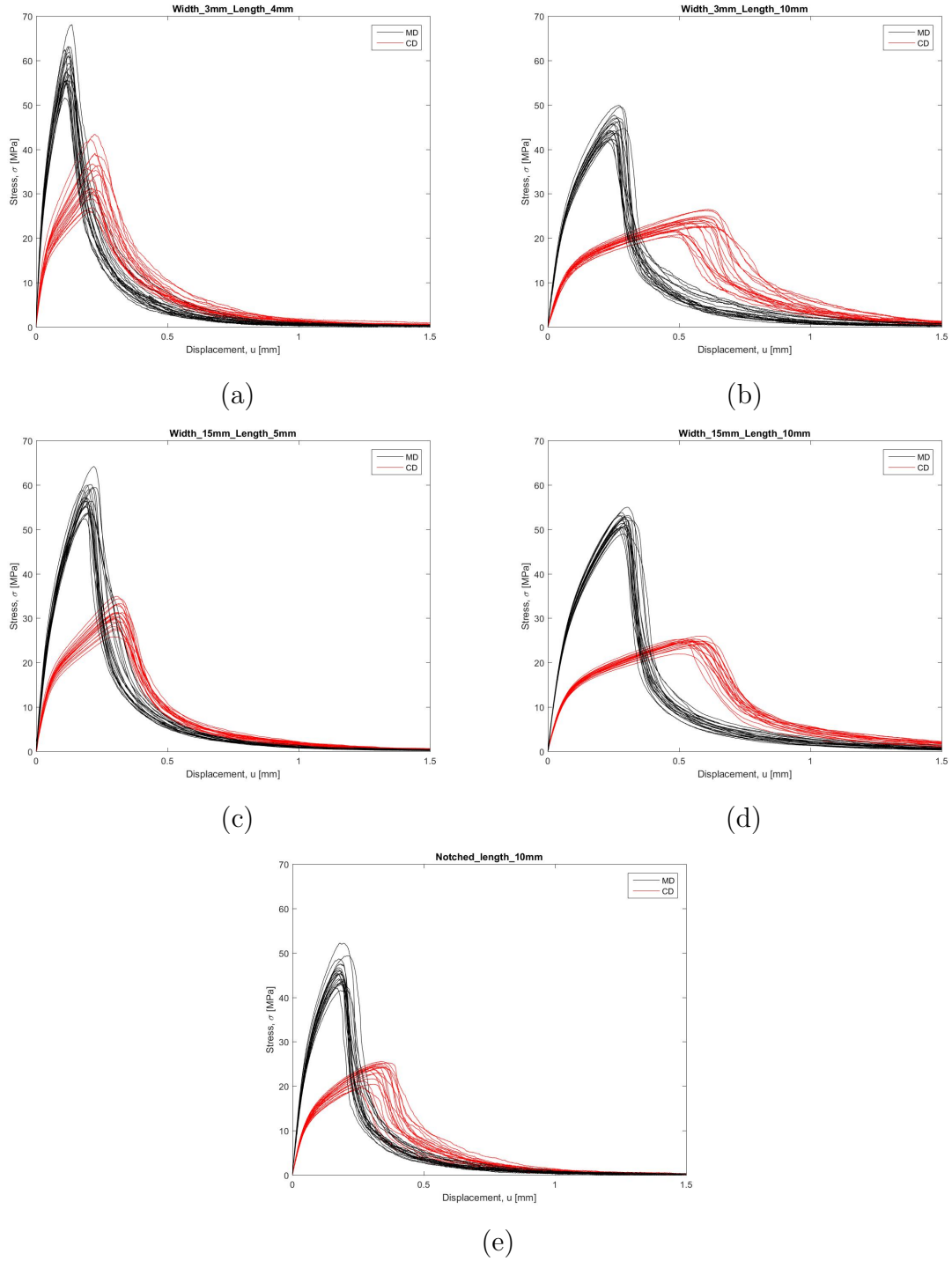
Figure 4.1: Results from the short-span tensile tests performed on paperboard samples with different geometries. (a) W=3 mm, L=4 mm, (b) W=3 mm, L= 10 mm, (c) W=15 mm, L= 5 mm, (d) W=15 mm, L= 10 mm, (e) W=3 mm at the notches, L= 10 mm.

All of the specimens exhibited a linear behaviour in the beginning of the curve, before entering a hardening zone. As may be seen in the shape of the graphs, all of

37

the specimens appear to undergo cohesive fracture after reaching the failure strength, which implies that the sample lengths are below L_{stable}. This was described in Section 2.1. For all of the tests performed the failure strength in CD is lower than the failure strength in MD. The corresponding displacement at failure strength is larger in CD compared to MD. The failure strength also decreases with increased length for both CD and MD. This was expected in accordance with the weakest link behaviour [15].

It can be noted that the spread of the stress-displacement curves in CD are greater for the specimens of width 3 mm compared to the specimens of width 15 mm. This is also true for the notched samples. Here the effective width of the samples between the notches was also 3 mm. The strain at failure appears to be the same for the samples of the same length but different widths. According to [13] the strain at failure is expected to be higher for wider specimens, but this is not observed in these experiments.

4.1.2 Cohesive stress-widening relations

From the stress-displacement curves in Figure 4.1 it was possible to construct cohesive stress-widening curves using Eq. (2.5). These curves can be seen in Figures 4.2 and 4.3, for MD and CD, respectively.
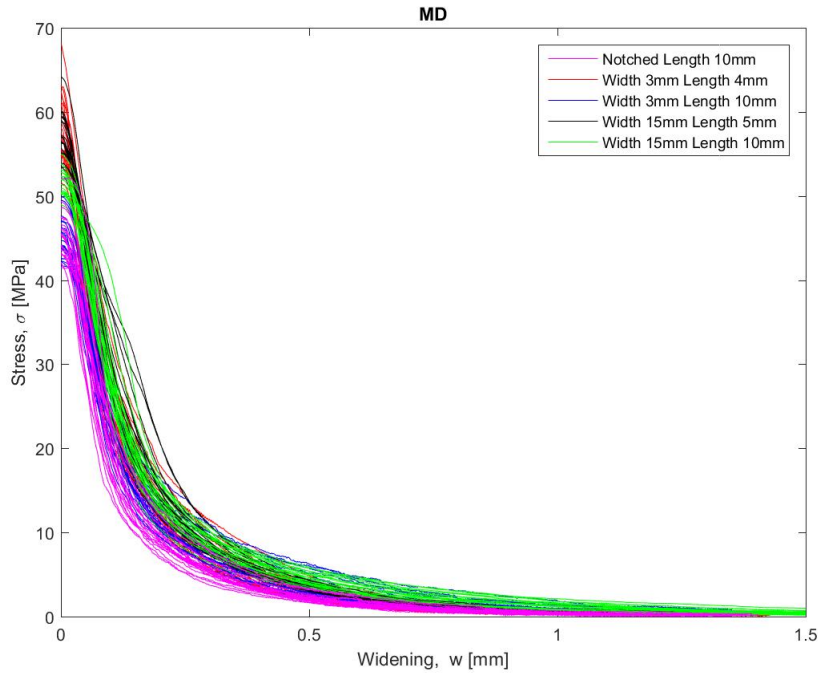

Figure 4.2: Cohesive stress-widening curves from the tensile experiments performed on paperboard in MD in the laboratory at Tetra Pak.
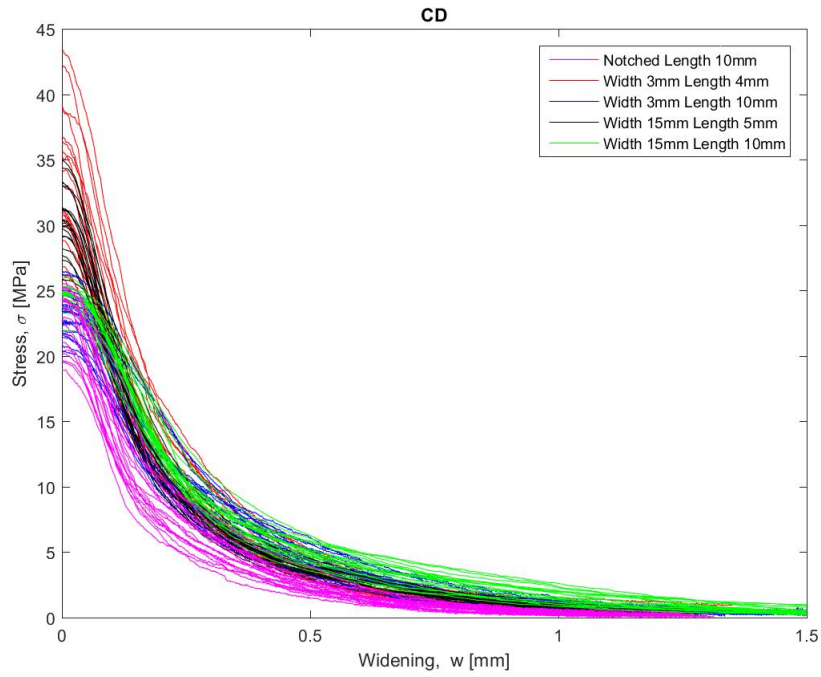
Figure 4.3: Cohesive stress-widening curves from the tensile experiments performed on paperboard in CD in the laboratory at Tetra Pak.

From Figures 4.2 and 4.3 it is shown that the cohesive stress-widening curves differ between the different samples, regarding the failure strength. According to [13], size effects are expected due to the differences in sizes and strain rates. The cohesive stress-widening curves were normalised and the results are displayed in Figures 4.4 and 4.5.
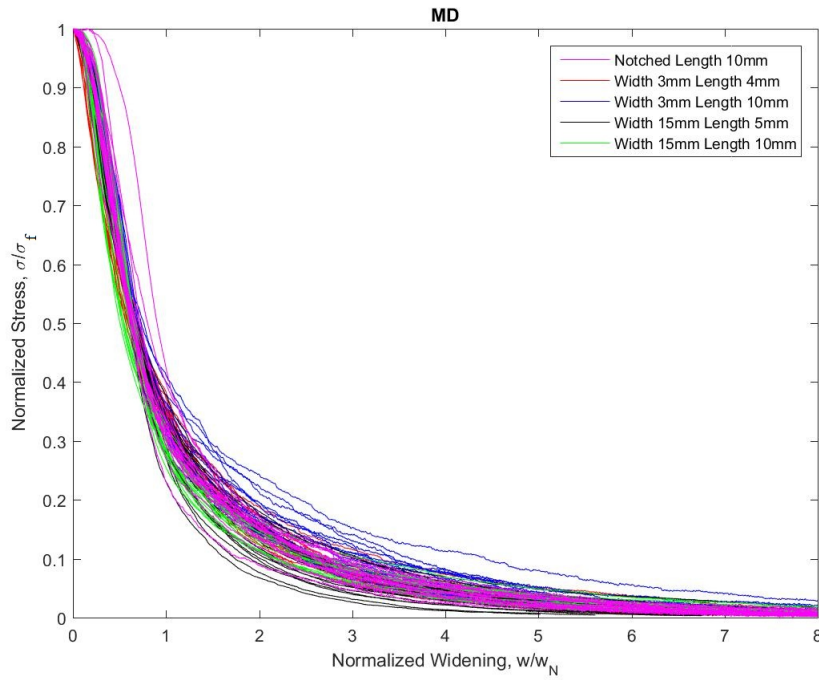
Figure 4.4: Normalised cohesive stress-widening curves from the tensile experiments performed on paperboard in MD in the laboratory at Tetra Pak.
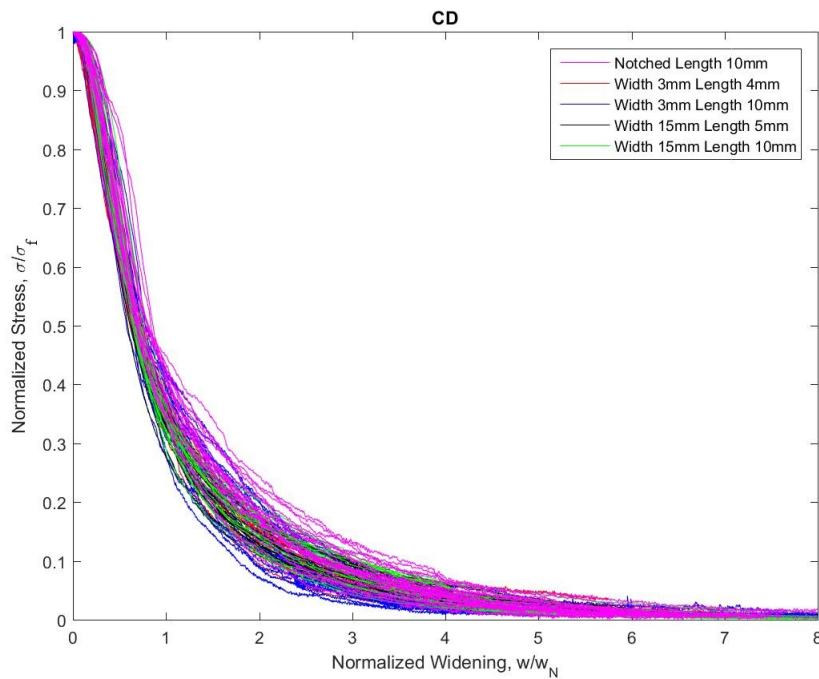

Figure 4.5: Normalised cohesive stress-widening curves from the tensile experiments performed on paperboard in CD in the laboratory at Tetra Pak.

The normalised cohesive stress-widening relations show that the curves follow the

same path regardless of size, strain rate and geometry. The spread of the curves is evenly distributed, hence, the characteristics of the shape of the curves are similar, independent of both geometry and strain rate.

4.1.3 Pre-delaminated cohesive stress relations

To investigate the impact of delamination on the cohesive stress-widening mechanism short-span tensile tests were performed. The results from pre-delaminated specimens were compared to the results from undamaged specimens.

The mean values and the standard deviation for the failure strength, the fracture energy and N_{max} are tabulated in Tables 4.1 and 4.2 for MD and CD, respectively.

Table 4.1: Mechanical parameters for both the pre-delaminated and undamaged specimens in MD. Mean: Geometrical mean, STD: Standard deviation.

	σ_f [MPa]		G_f [MPa*mm]		N_{max} [MPa/mm]	
	Pre-Del.	Undamaged	Pre-Del.	Undamaged	Pre-Del.	Undamaged
Mean	54.6	58.0	10.2	9.8	308.6	394.8
STD	1.9	3.0	1.0	1.1	53.0	105.4

Table 4.2: Mechanical parameters for both the pre-delaminated and undeformed specimens in CD.

	σ_f [MPa]		G_f [MPa*mm]		N_{max} [MPa/mm]	
	Pre-Del.	Undamaged	Pre-Del.	Undamaged	Pre-Del.	Undamaged
Mean	28.6	31.2	6.8	7.2	136.4	146.3
STD	1.2	1.9	0.4	0.5	15.9	13.4

The mean failure strength for the pre-delaminated specimens is 5.9 % lower in MD and 4.1 % higher in CD compared to the undamaged specimens. On the other hand the standard deviation is greater for the undamaged samples, 3 MPa (MD) and 1.9 MPa (CD), compared to the pre-delaminated specimens of 1.9 MPa (MD) and 1.2 MPa (CD). By performing a paired t-test, the null-hypothesis that the pairwise difference between the failure strength for the pre-delaminated and the undamaged specimens has a mean equal to zero [27]. The hypothesis was true on an significance level of 1% for MD and rejected for CD.

By performing a paired t-test for the fracture energy and the maximum slope of the stress-displacement curve, N_{max}, the null-hypothesis was true on a significance level of 1% for both MD and CD.

4.2   Tomograph experiments

The experiments in the tomograph were performed in an uncontrolled environment. However, the relative humidity is reported to not affect the shape of the normalised cohesive stress-widening curve. Furthermore, the displacement rate also differed compared to the experiments performed in the laboratory at Tetra Pak, but this effect is also cancelled out when the curves are normalised [18]. Comparing the tensile experiments performed in the tomograph with the tests in the laboratory at Tetra Pak there are some differences that have to be taken into account. Firstly, it should be noted that even though the geometry of the clamps used in the tomograph may not be exactly the same as for the ones used in the laboratory at Tetra Pak, the impact of this on the result is assumed to be negligible. Secondly, to be able to compare the results from the tomograph with the results from the laboratory at Tetra Pak the cohesive stress-widening curves had to be normalised, as was described in Section 2.1.

4.2.1   Short-span tensile tests with notched samples

In Figure 4.6 (a) the results from the short span tensile tests performed with the equipment used in the tomograph is shown. The experiments were performed at the Lund University site but not in the tomograph. In Figure 4.6 (b) the tensile tests performed with the notched samples at Tetra Pak are shown. The samples in Figure 4.6 (a) and (b) had the geometry of test sample 5 in Table 3.1.

The results in Figure 4.6 (a) show a spread of the data that is significantly higher and a failure strength that is overall lower compared to the experiments performed at Tetra Pak, shown in Figure 4.6 (b).

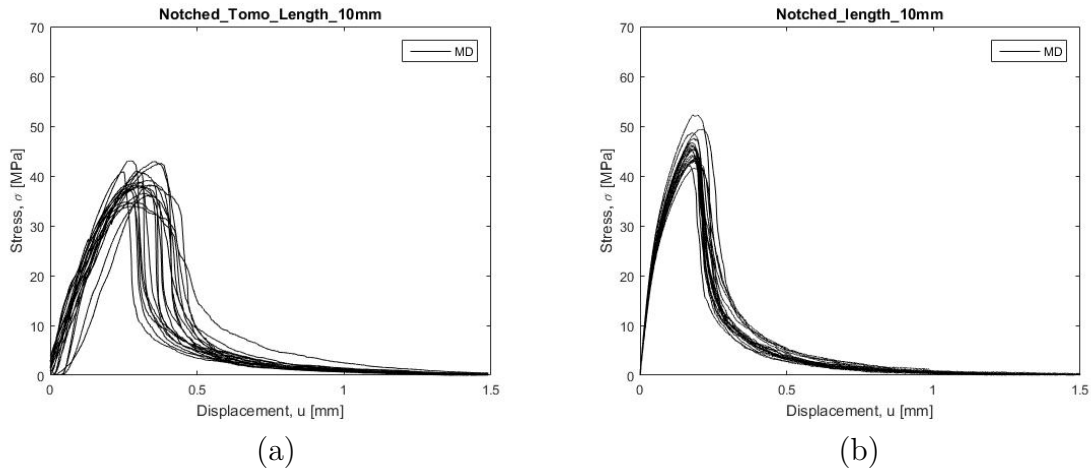(a)   (b)

Figure 4.6: (a) Stress-displacement curves for the notched specimens using the tomograph tensile tester. (b) Stress-displacement curves for the notched specimens using the tensile tester in the climate controlled laboratory at Tetra Pak. The samples in both (a) and (b) had the geometry of test sample 5 in Table 3.1.

Figures 4.7 and 4.8 show the cohesive stress-widening curves and the normalised co-

hesive stress-widening curves in MD when also the experiments performed in the tomograph tensile tester are included. In Figure 4.7, differences regarding failure strength and the overall shape of the curves are shown. This was expected due to the different geometries, moisture contents and strain rates. In Figure 4.8 the cohesive stress-widening curves from Figure 4.7 have been normalised to eliminate these effects. It is shown that the experiments performed in the tomograph tensile tester setup have a spread that is larger than the tests performed at Tetra Pak, even after normalisation. However, the results from the tomograph tensile tester shows that the majority of the curves have a shape similar to the curves from the experiments performed at Tetra Pak. Hence, it is assumed that the mechanisms that are observed in the tomograph are the same as for the tests performed at Tetra Pak.
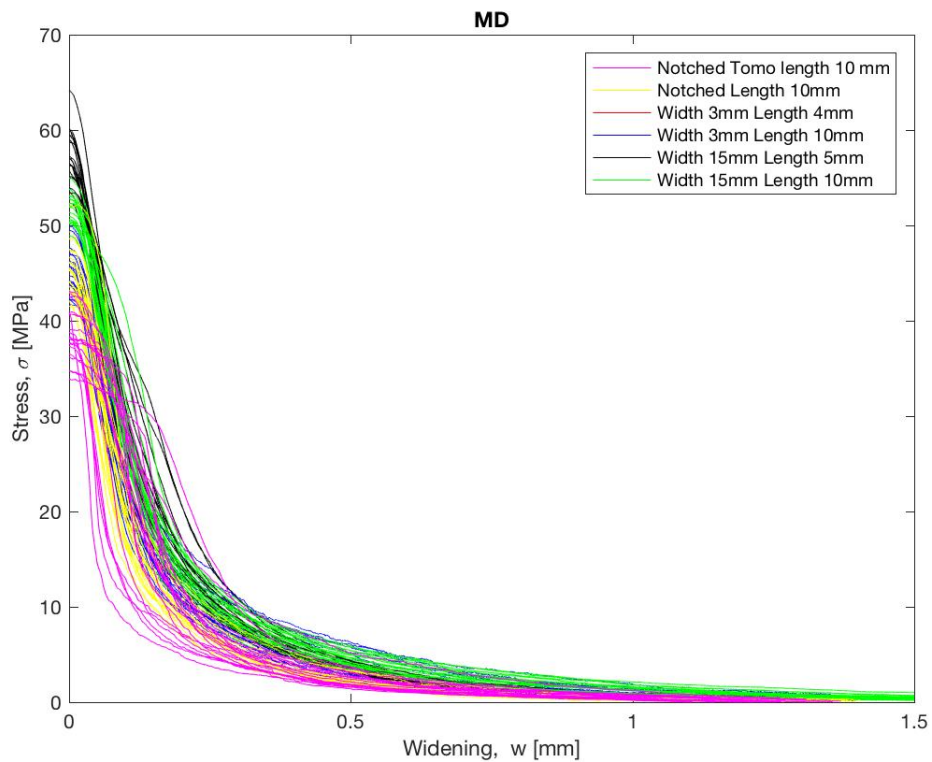

Figure 4.7: Cohesive stress-widening curves in MD for all tests, including both the tests performed at Tetra Pak and at Lund University.
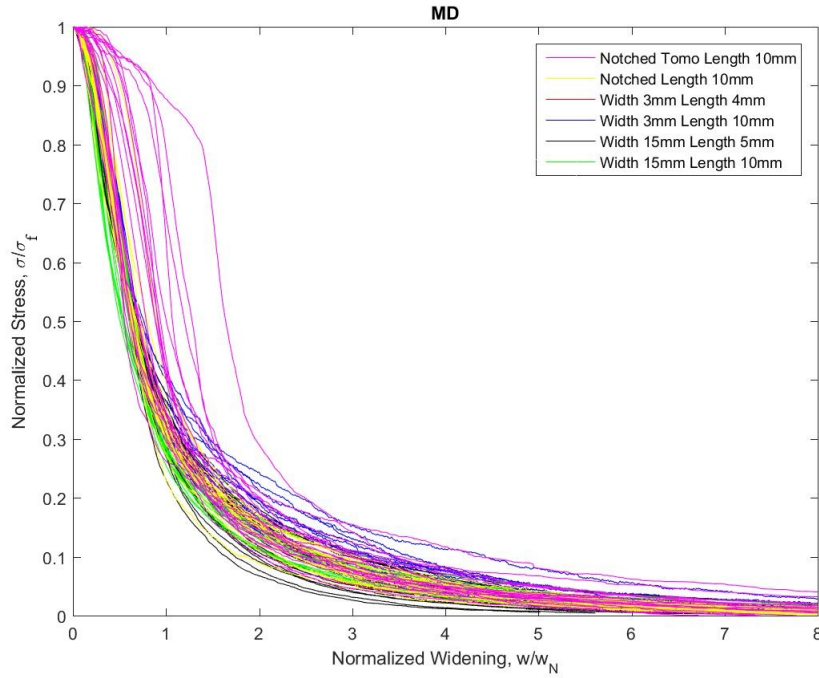
Figure 4.8: Normalised cohesive stress-widening curves in MD for all tests, including both the tests performed at Tetra Pak and at Lund University.

4.2.2   In-situ stress-displacement curve in the tomograph

From the experiments in the tomograph, Figure 4.9 (a) was constructed. The vertical drop in load at holding points 2-6 is due to relaxation of the specimen. Furthermore, the straight horizontal lines after point 2, 3 and 5 indicate that the measured data are disturbances from the sensor measuring the displacement. These disturbances mean that the sensor measured a displacement that in reality did not exist. However, this will not affect the images generated by the tomograph. The reason for the negative stress at holding point 6 has to do with the zeroing of the stress at the start of the test. The zeroing was performed when it was some positive tension in the specimen causing the displayed stress to be lower than the actual stress acting in the specimen. Note that the black line that goes straight down at the failure strength at holding point 5 is due to the fact that the experiment was stopped at this point, and is due to the relaxation. Hence, this is not a brittle failure. The test was finished at a smaller displacement compared to the ordinary short-span tensile tests.

By comparing the curve from the experiment in the tomograph with one of the curves from the short-span tensile tests performed with the same tensile tester (Figure 4.9 (b)), it may be seen that the relaxation does not affect the results that much, cf. Figure 4.9. The failure strength occurs at roughly the same displacement, and is approximately of the same magnitude. The disturbances from the displacement sensor however causes the measured displacement to differ from the actual displacement.
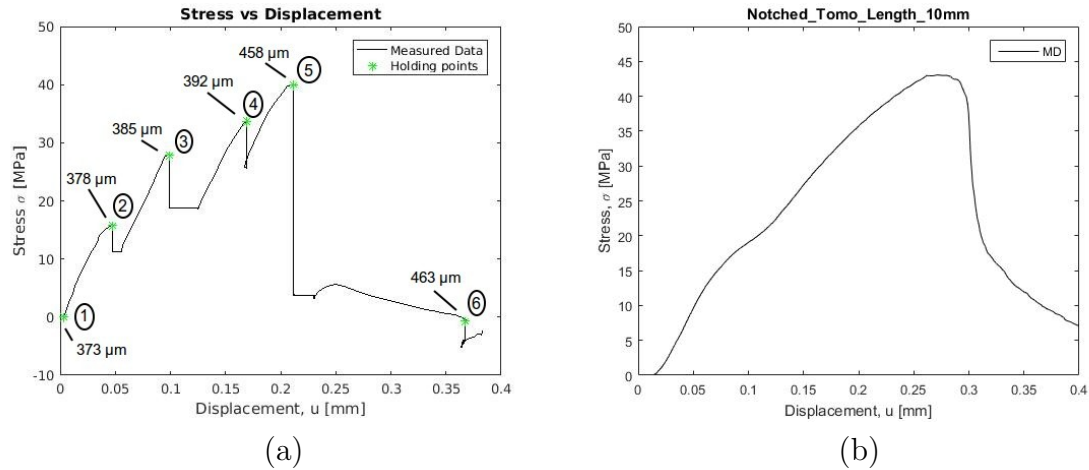
Figure 4.9: (a) Stress-displacement curve from the tensile experiment in the tomograph, including the different holding points and the thickness of the paperboard specimen at each holding point. (b) One of the curves from Figure 4.6 (a) for continuous, monotonic loading in the tomograph loading device (i.e. without stopping for scans).

4.3   Image analysis

The three dimensional images obtained from the tomograph consisted of a large number of slices through the internal structure. Images with different views for each holding point are displayed in this section. The three dimensional images obtained from the tomograph had a voxel count of 998 in MD, 988 in CD and 1014 in ZD and each voxel corresponded to a cube with sides of 3.5 μm.

In Figures 4.10-4.15 images showing the internal structure at the holding points 1, 2, 3, 4, 5 and 6 are displayed. The cross in each image corresponds to the position within the specimen currently in view. The top left image (A) corresponds to a view of the specimen seen from the front, top right (B) as seen from the side and bottom left (C) as seen from the top. Note that these images are colour scaled using the software Fiji to get clearer images.
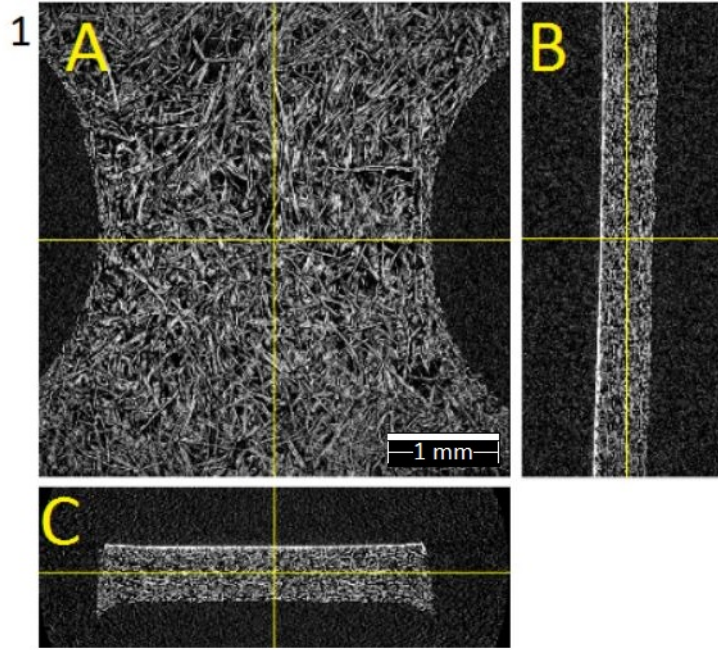
Figure 4.10: Tomograph image of the reference specimen, holding point 1.
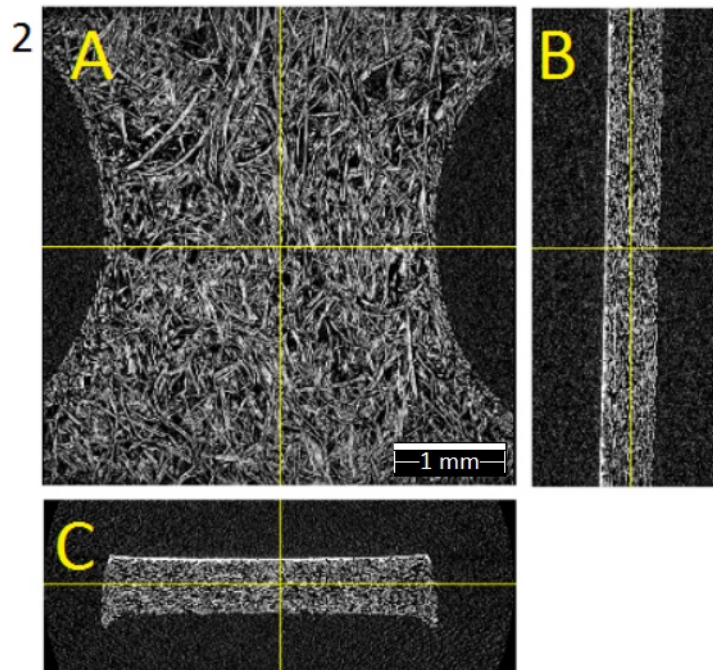

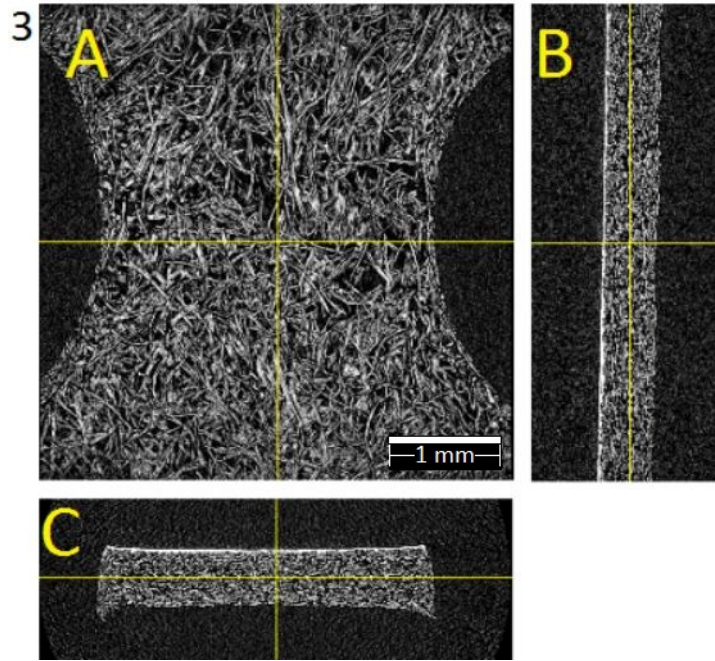Figure 4.11: Tomograph image of the specimen at holding point 2.

Figure 4.12: Tomograph image of the specimen at holding point 3.
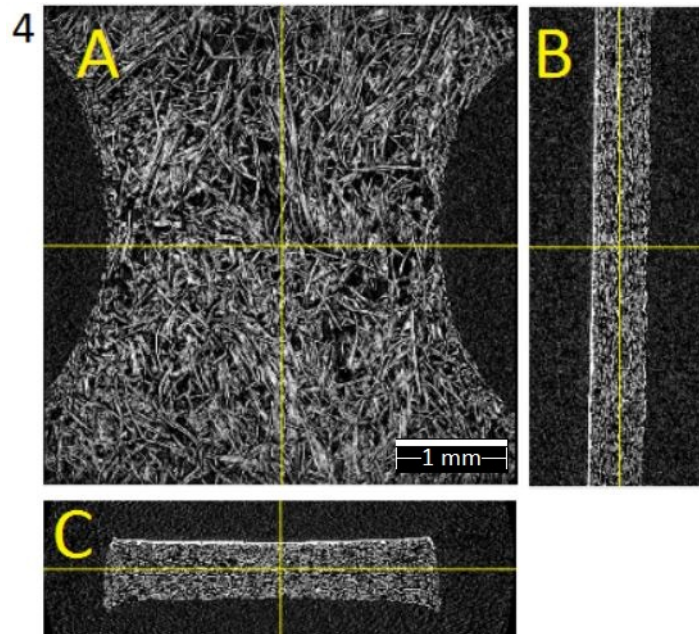

Figure 4.13: Tomograph image of the specimen at holding point 4.
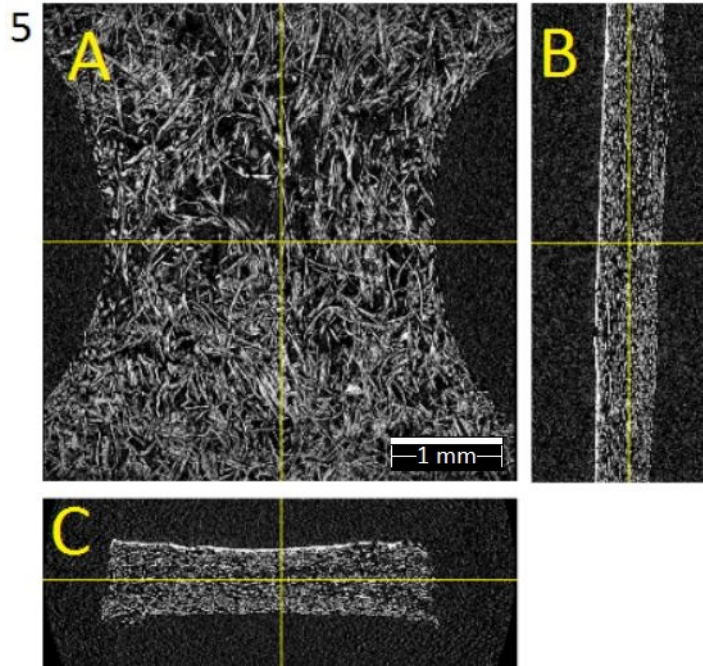
Figure 4.14: Tomograph image of the specimen at holding point 5.
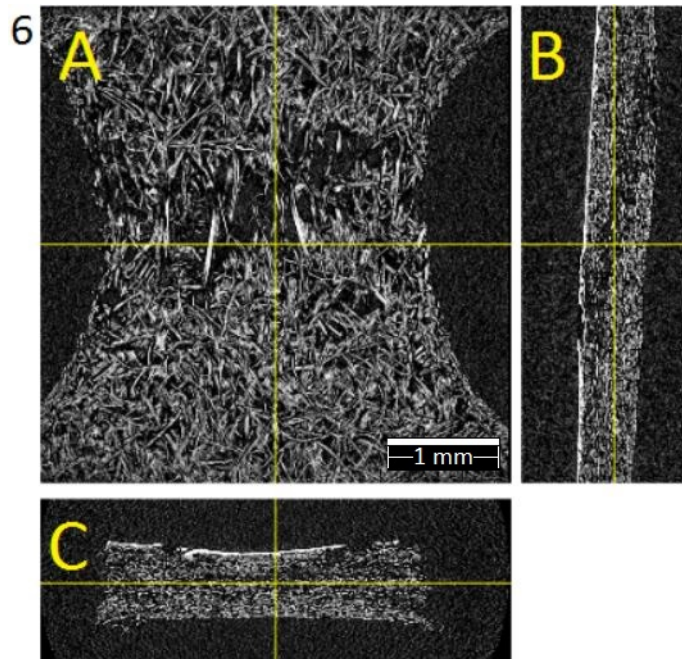
Figure 4.15: Tomograph image of the specimen at holding point 6.

The bright network that is visible within the structure in Figures 4.10 - 4.15 are the fibres. The darker parts correspond to air, where no fibres exist. The white edge that can be seen in the B and C images corresponds to the clay coating.

In Figure 4.10 A, the image for the undamaged specimen, it can be seen that at the notches the fibres are shorter compared to other locations within the specimen.

This is due to the cutting process of the sample.

No changes are visible when comparing the images between holding points 1-4. To study the small changes that might occur between the images the analysing tool DVC is used. At holding point 5 (Figure 4.14) structural changes start to become visible. Large voids are forming in images A, B and C. By looking at image B it can be seen that the localised failure zone stretches diagonally through the sample. Furthermore, by looking at image A, it can be seen that the localised failure zone forms in the notch as expected, due to the smaller area in this section. At holding point 6 (Figure 4.15) voids become even clearer and the localised damage zone can be seen to widen diagonally through the sample.

The images in Figure 4.16 were constructed using Fiji. The images show the mean intensity of the projection along each line of voxels in the CD-direction. The yellow line corresponds to the section over which the thickness of the sample was measured. Note that the mean intensity was used, and hence thickness variations that only span over a few slices will not show, since the black background that spans over the rest of the slices will lower the mean intensity. The measured thickness for each holding point is shown in Figure 4.9. Note that the clay coating was not included in these measurements, since the thickness of the sample after failure would be hard to measure otherwise.
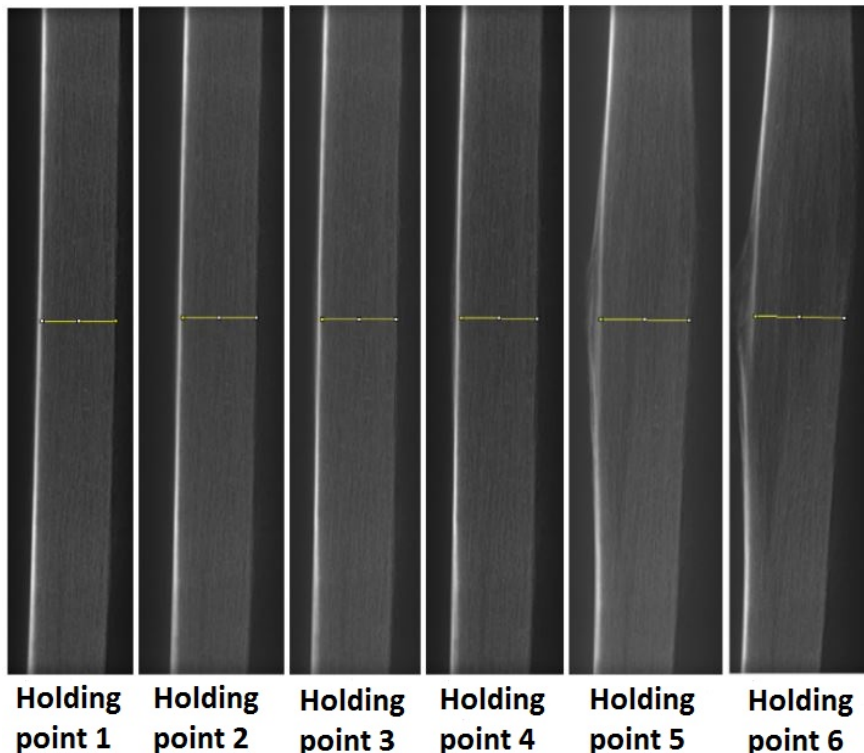

Figure 4.16: Figure showing the specimen from the side, using the mean intensity through its side. The yellow line corresponds to the section where the thickness was measured.

In Figure 4.17 the thickness as a function of displacement is shown. Loading leads to an increase of thickness as a function of displacement. Note that the thickness is only known at the holding points. More points of investigation would be beneficial since this would have made it possible to investigate the development of the specimen with more accuracy. This is especially true close to the failure strength, since the thickness increases rapidly close to this point.

Figure 4.17 shows that the thickness of the sample increases immediately after the specimen is subjected to load, and keeps increase throughout the test. For holding points 1-4 the thickness increase is around 5 to 7 μm between each holding point. However, between holding points 4 and 5 the increase is larger, 66 μm. After failure the thickness increase is once again 5 μm. These observations alter some in comparison to what Gabrielsson (2017) observed, where thickness increase was only observed after failure strength [19]. It should be noted that the paperboards used in the experiments of Gabrielsson was not the same as the ones used in the experiments reported herein.
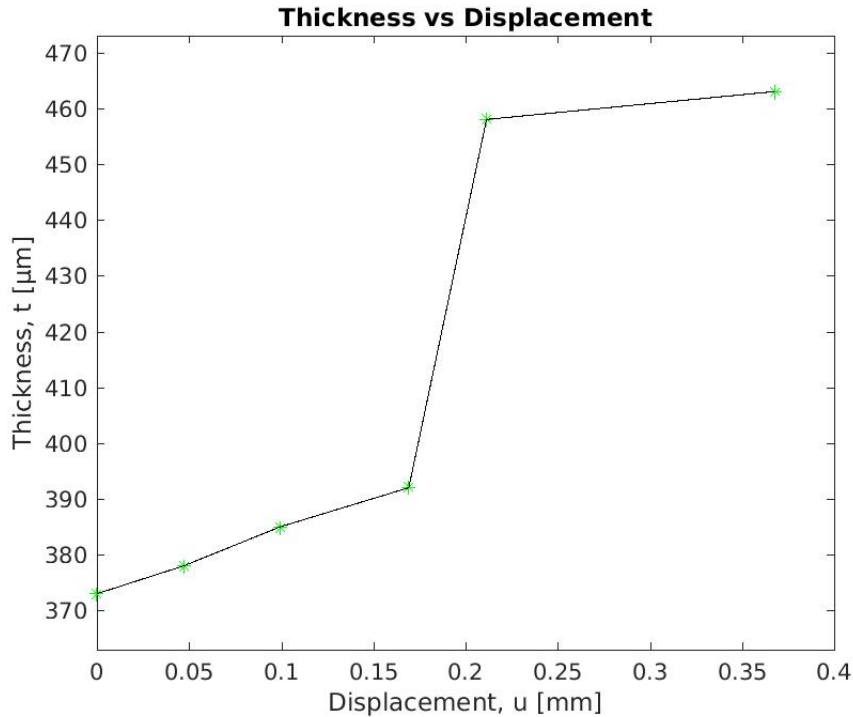

Figure 4.17: Thickness as a function of displacement for the analysed paperboard sample. The green points corresponds to the holding points.

4.4 Digital Volume Correlation (DVC)

By using DVC it was possible to get an insight into what occurred within the material upon loading. By just visual inspection of the tomograph images it was difficult to come to any conclusions about the material behaviour. Hence, further quantifiable image analysis was done. As described in Section 3.3, digital volume correlation was performed using the TomoWarp2 DVC program, written in Python. This provided displacement fields and strain fields. Since the coordinate system in the tomograph was reset between each holding point the displacement fields included rigid body motions. However, rigid body motion does not affect the strain fields. The strain fields in the following section are the strains between each holding point, and not the total strains. Since the displacements between each holding point are different the amount of strain between each holding point should be compared with caution. Note that the centre of the colour scale in the following strain fields do not always correspond to zero.

As was mentioned by Hall, Viggiani and Romero (2012) [24] certain problems using DVC may occur due to the steps of only total voxels in displacement, generating a low sub-voxel resolution, (see Section 2.2.2). Even though precautions have been made to minimise this with sub-voxel refinement, certain artefacts in the images from the DVC analysis may still be present due to this. These artefacts may be hard to distinguish from real results, but certain behaviour may give it away. For example certain patterns, like circular rings or when the strain value goes from high, to low, to high in a repetitive pattern it might be an indication of an artefact.

4.4.1 Strain fields

As described earlier all normal- and shear strain fields (i.e. the full three dimensional tensor strain field), were calculated. In Figure 4.18 the coordinate system and geometrical information for the setup can be seen.
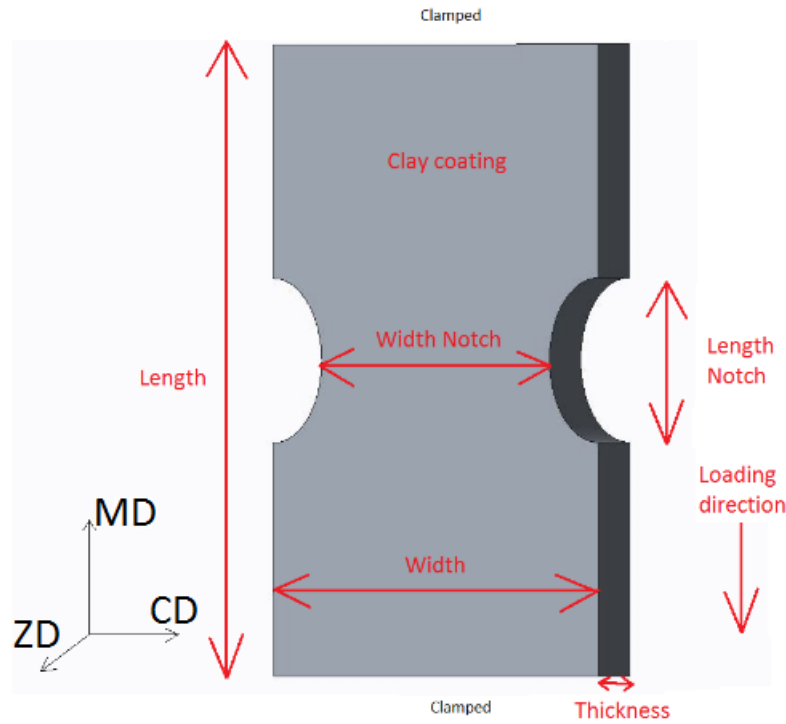
Figure 4.18: Schematic image of the specimen showing the coordinate axes, measurements and boundary conditions.

Six holding points generated six three dimensional images from which displacement fields in the three orthogonal directions could be analysed between each holding point. TomoWarp2 also provided the full three dimensional strain tensor field. However, when analysing the strain fields it was noted that the digital volume correlation did not work after failure. This was due to the fact that the displacement was large and much was happening in the material at this point, which meant that the result from the DVC analysis was unusable. This further means that the strain fields between holding points 5 and 6 were not analysed. All strain fields between the rest of the holding points are commented upon. The mean value of the correlation coefficient, which is a measurement of how well the DVC program is able to match the voxels between two 3D-images, was between 99.31-99.48 % between all holding points.

In Figures 4.19-4.32 different strain fields are shown. View A corresponds to the sample seen from the front, looking in the thickness direction (ZD). View B corresponds to the sample seen from the side looking in the width direction (CD), and view C corresponds to the sample seen from the top, looking in the loading direction (MD).

4.4.1.1   Normal strains

Strains in CD (ϵ_{CD}):

In Figures 4.19 and 4.20 the normal strains in CD between holding points 3 to 4 and 4 to 5 are shown, respectively.

The strain field in view A in Figure 4.19, shows larger strains at the notches compared to the rest of the sample. By analysing different slices through the thickness it was seen that the observed strains were the same through the entire thickness of the sample. The ϵ_{CD}-field shown in Figure 4.19 are similar to the ϵ_{CD}-fields between holding points 1 to 2 and 2 to 3 respectively, these strain fields can be seen in Appendix C.

Besides the strain concentration at the notches, the ϵ_{CD}-field is low and reasonably homogeneous for all the views (A, B and C). Furthermore, after failure strength, when the failure zone has been initiated, the higher strains at the notches no longer exist. Instead widening of the cohesive failure zone occurs, which was expected due to the theory of how the failure zone evolves in paperboard [3]. When analysing the tomograph images it was observed that the widening of the failure zone was localised diagonally through the sample which can be seen in all the strain fields between holding points 4 and 5.
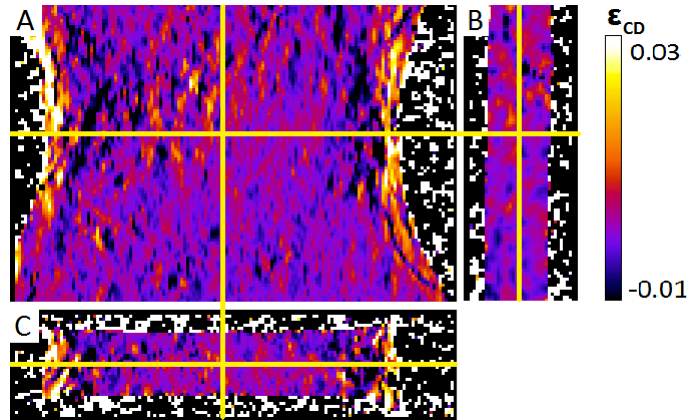

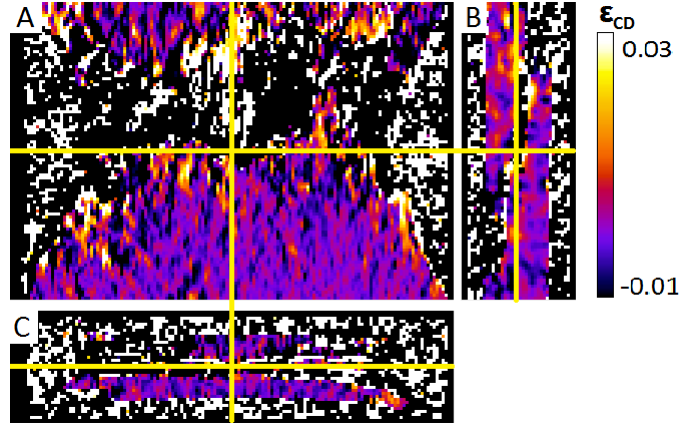Figure 4.19: Strain field in CD between holding points 3 and 4.

Figure 4.20: Strain field in CD between holding points 4 and 5.

Strains in ZD (ϵ_{ZD}):

In Figures 4.21 - 4.24 the normal strains in ZD for all holding points are shown. In view A, it is possible to see that the strains are localised between the notches all the way from holding points 1 to 5. This was more or less expected, since the smaller cross sectional area should lead to stress concentration and hence also strain localisation. It should be noted that the strains in ZD are present already at the first holding point, which should indicate a dilation of the sample the entire way from loading start to failure. This was also observed in Figure 4.17 where the thickness change of the sample was measured.

For the strain fields in view B, it is possible to see strain localisation through the length of the specimen. This localisation is obvious already between holding points 1 and 2, and remains in the middle of the sample all the way to failure. This means that it is only the middle of the sample that contributes to the thickness increase that was observed in Figure 4.17. This becomes even clearer if the strain fields between holding points 3 and 4 are studied where three images can be seen. These are different slices in the thickness direction. The first image (α) corresponds to a slice close to the clay coating of the sample, the second image (β) to a slice in the middle of the sample in the thickness direction and the third image (γ) to a slide close to the side opposite of the clay coating. By comparing (α), (β) and (γ) it is even more noticeable that the strains are localised in the middle of the sample (image (β)) in ZD. Note that it is image (β) between holding point 3 and 4 that should be compared to the rest of the strain fields in ZD since those images are taken from the middle slice.

By analysing the strains of the sample in view A in Figure 4.23, it can be seen that in image (α) the strains are somewhat localised at the bottom part of the sample, in image (β) they are higher and perhaps somewhat localised at the top of the sample while in image (γ) they are localised at the notches and then seems to follow a parabolic pattern. If these three images are compared to Figure 4.24 (image B) where it is seen that the failure zone travels diagonally through the sample a connection can

be seen. If the first slice in Figure 4.23 (image α), where the strains are localised at the bottom in view A are compared to view B in Figure 4.24 a relation can be seen. It is at the same place where the strains are high between holding points 3 and 4 where also the failure zone later propagates. This is also true for image (β) and (γ). This indicates that the diagonal direction of the failure zone is connected to the strains in ZD.

By comparing the strains in view C for all holding points, it is possible to see a change of strain localisation. At first, the strains appear at the notches, but spread inwards with increasing load. This has to do with stress concentrations at the notches.
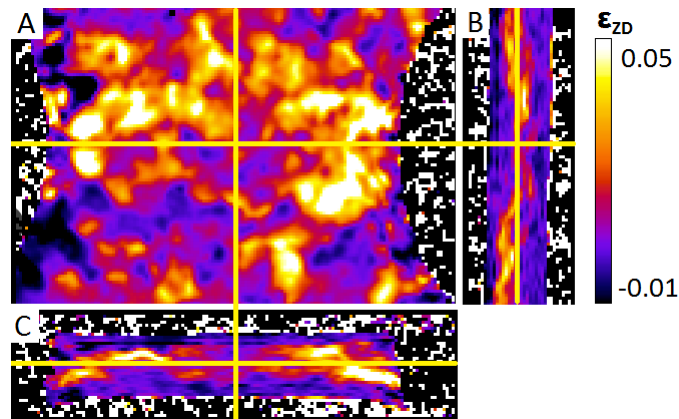

Figure 4.21: Strain field in ZD between holding points 1 and 2.
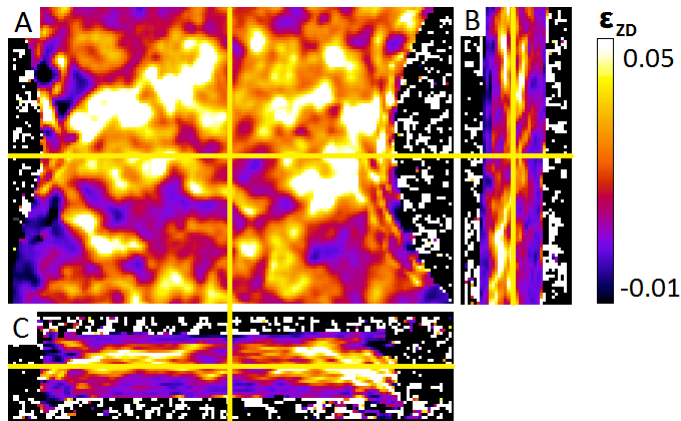

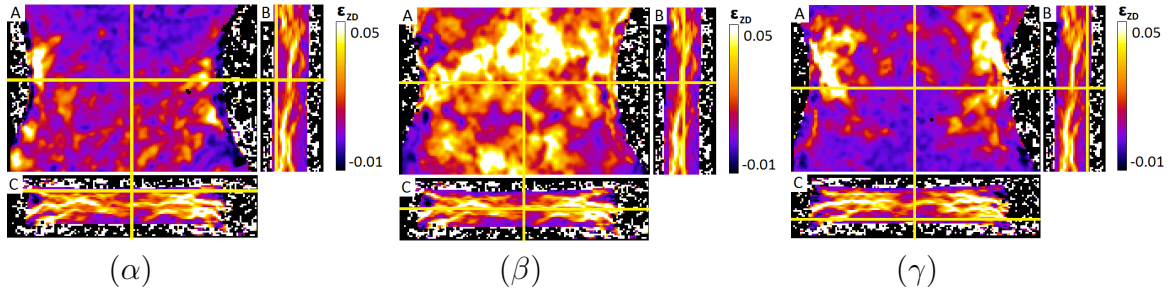Figure 4.22: Strain field in ZD between holding points 2 and 3.

Figure 4.23: Strain fields in ZD for holding points 3 to 4. (α) shows a slice at the end of the sample in the thickness direction, close to the clay coating, (β) shows a slice at the middle in the thickness direction and (γ) shows a slice at the opposite side of the sample compared to (α).
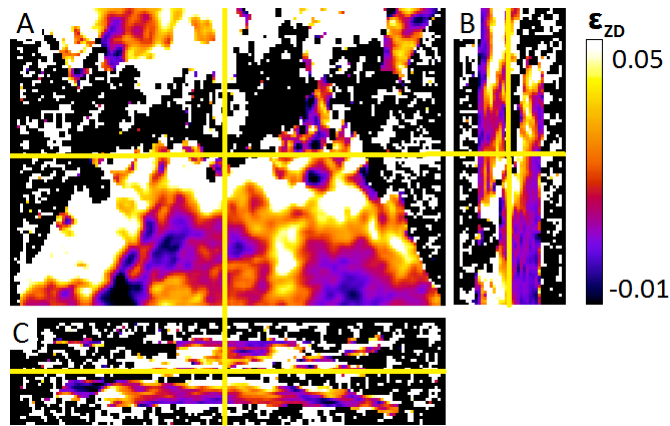

Figure 4.24: Strain field in ZD between holding points 4 and 5.

Strains in MD (ϵ_{MD}):

In Figures 4.25 - 4.28, the strains in MD between all holding points are displayed. The strains are localised at the notches, which may be seen already between holding points 1 and 2 in view A. Zones with higher strains exist and they evolve in a somewhat parabolic pattern between the notches. They are visible all the way from loading start but become more clear between holding points 3 and 4. Besides the higher strain zones, somewhat uniform strain is present in the whole analysed area between holding points 1-4, and may be seen in all the views. When failure has occurred, the strains are localised in close proximity to the notch while it is close to zero in the rest of the sample. This pattern is present in especially view A an B.

Note that the dark lines present in the top of Figure 4.25 and 4.26 in view A and B most likely are artefacts from the DVC analysis.
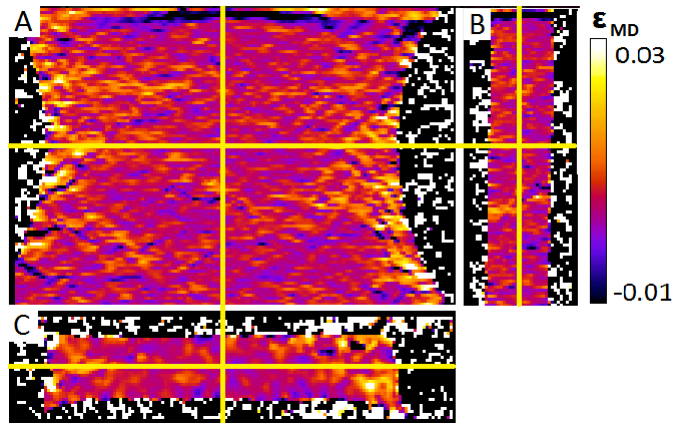
Figure 4.25: Strain field in MD between holding points 1 and 2.
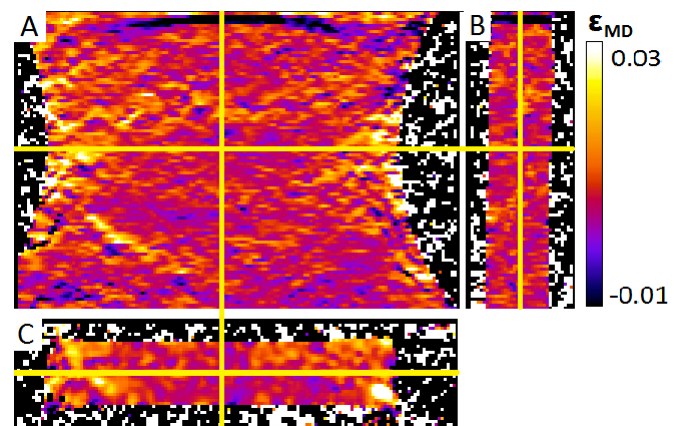

Figure 4.26: Strain field in MD between holding points 2 and 3.
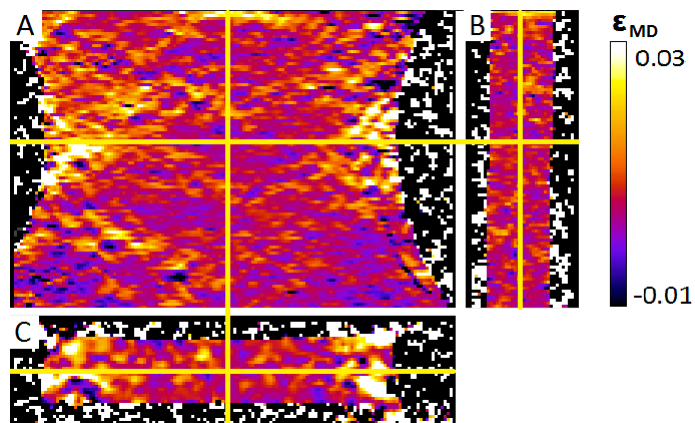

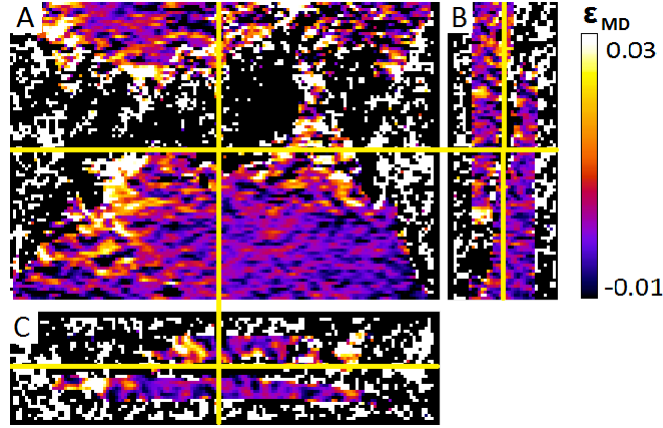Figure 4.27: Strain field in MD between holding points 3 and 4.

Figure 4.28: Strain field in MD between holding points 4 and 5.

4.4.1.2 Shear strains

The shear strains, ϵ_{CDMD}, ϵ_{CDZD} and ϵ_{ZDMD} were also analysed. Note that all strains refer to the coordinate system described in Figure 4.18. All shear strain fields can be seen in Figures 4.29 - 4.32 where each figure corresponds to strain fields between different holding points. The α images display the ϵ_{CDMD}-field, the β images display the ϵ_{CDZD}-field and the γ images display the ϵ_{ZDMD}-field.

Note that the scales in Figure 4.32 differ compared to the other figures. This is due to the fact that the ϵ_{ZDMD}-field became much larger here than between the previous holding points which made the change in scale necessary to be able to visualize the results.

When analysing the strain fields between holding points 1 and 2 it can be seen that the ϵ_{CDMD}-field is homogeneous and close to zero. In the ϵ_{CDZD}-field the strains varies a bit more, being negative or close to zero with some zones with higher strain present. The ϵ_{ZDMD}-field undergoes a change when comparing the top of the sample with the bottom in view A, going from negative to positive. Zones with higher strains are present in the lower part as well as in the upper part. In view C strain localisation at the notches can be seen.

Between holding points 2 and 3 the ϵ_{CDMD}-field is still relatively homogeneous with somewhat more negative values compared to the ϵ_{CDMD}-field between holding points 1 and 2, however this change is rather small. The ϵ_{CDZD}-field in Figure 4.30 overall stays the same, with zones of higher strains present at the same places as before. Regarding the ϵ_{ZDMD}-field in the same figure, the negative strains in the top no longer exist, but instead are mostly close to zero or somewhat positive in view A. The same can also be seen in the view B. The C view remains the same with localisation at the notches. Overall the zones of higher strain that were present in Figure 4.29 are also present in Figure 4.30.

Between holding points 3 and 4, the ϵ_{CDMD}-field remains rather constant in all views

58

and the ϵ_{CDZD}-field looks overall the same as between holding points 2 and 3. Regarding the ϵ_{ZDMD}-field in Figure 4.31 the strain localisation as was seen in view A in Figure 4.30 remains but with somewhat higher strains in the middle of the sample and somewhat lower strains at the bottom.

Between holding points 4 and 5, failure occurs. In the ϵ_{CDMD}-field this shows in a sudden positive strain present in the whole sample, in all the views. Noticeable is that in view B, the left part of the sample gets a more positive shear strain. This is also seen for the top part in view C. In the ϵ_{CDZD}-field negative shears are present in view A, close to the notches and when looking at view B it can be seen that the left part of the sample gets a more positive shear strain than the right part. Also, in view C it is possible to see that the upper part gets a higher value than the bottom part. Regarding the ϵ_{ZDMD}-field, it is seen that the strains close to the failure zone are highly positive, while they are negative some distance away from it as seen in view A. Furthermore, in view B it is seen that the strains in the left- and right part differs. The same can be seen for the strains in the top- and bottom part in view C.

(α) $\qquad$ (β) $\qquad$ (γ)
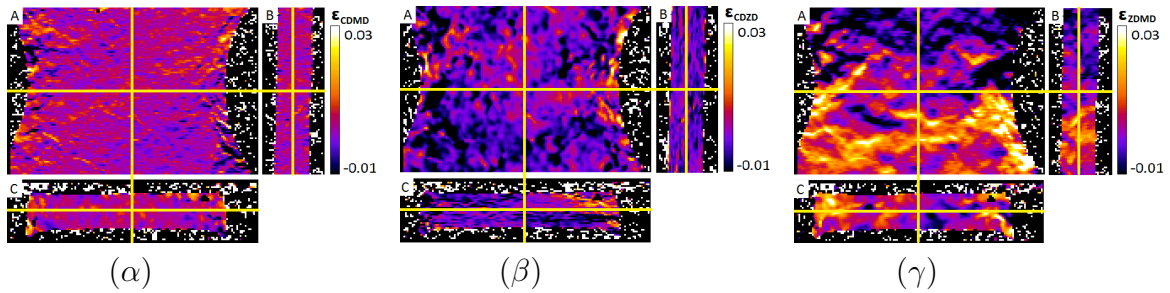
Figure 4.29: Strain field between holding points 1 and 2, ϵ_{CDMD}-field (α), ϵ_{CDZD}-field (β) and ϵ_{ZDMD}-field (γ).

(α) $\qquad$ (β) $\qquad$ (γ)
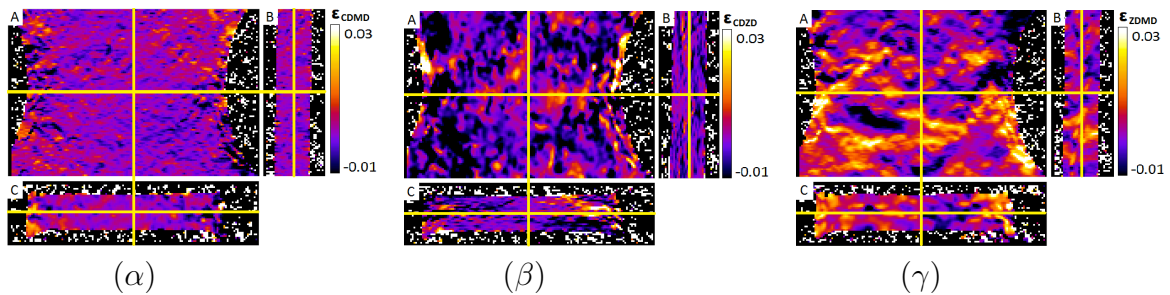
Figure 4.30: Strain field between holding points 2 and 3, ϵ_{CDMD}-field (α), ϵ_{CDZD}-field (β) and ϵ_{ZDMD}-field (γ).
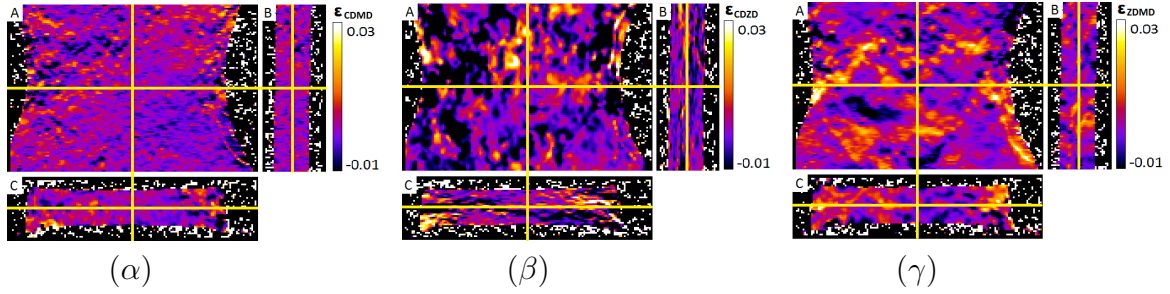
Figure 4.31: Strain field between holding points 3 and 4, ϵ_{CDMD}-field (α), ϵ_{CDZD}-field (β) and ϵ_{ZDMD}-field (γ).
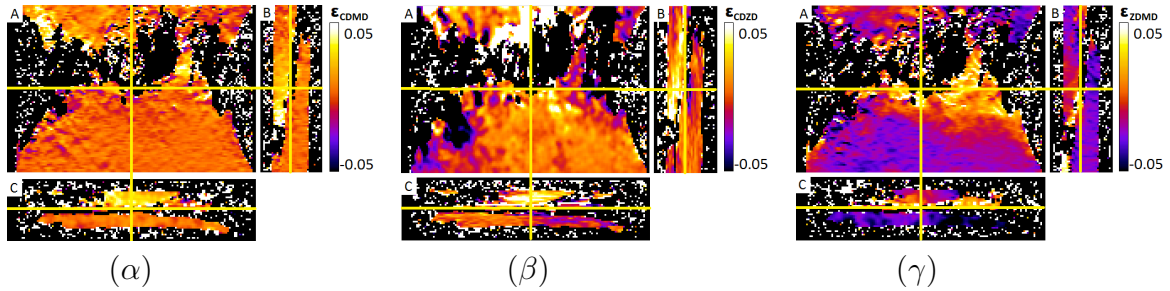
Figure 4.32: Strain field between holding points 4 and 5, ϵ_{CDMD}-field (α), ϵ_{CDZD}-field (β) and ϵ_{ZDMD}-field (γ).

4.5 Summary

In this chapter, the curves from the tensile experiments performed on different geometries have been compared and the tomograph images have been displayed. Observations from the tomograph images as well as from the strain fields provided by the DVC program TomoWarp2 have also been commented upon. In the next chapter the experimental results are further discussed together with conclusions and suggestions for further work.

CHAPTER 5

Discussion, conclusions and further work

5.1 Discussion

For experiments where only a tensile tester is used, the only information obtained is
the stress-displacement curves. When x-ray tomography is added, it gives the possi-
bility to get three dimensional images of the structure of the material. Due to this,
it is possible to analyse the internal structure of the paperboard during tensile load-
ing. By also applying digital volume correlation it is possible to analyse strains on a
quantitative manner.

From the short-span tensile tests performed in the laboratory at Tetra Pak it is seen
that the geometry of the sample affects the mechanical properties regarding the fail-
ure strength and failure strain. The normalised cohesive stress-widening curves from
the short-span tensile tests showed that, even though the geometries varied, the same
cohesive behaviour was observed. By performing short-span tensile tests where both
the climate and the strain rate differed from the laboratory at Tetra Pak, it was con-
firmed that after normalisation the cohesive stress-widening curves were independent
of these parameters. This indicated that the mechanisms observed in the tensile test
performed in the tomograph for which notches were introduced are representative for
this paperboard in general.

For the short-span tensile tests performed with the tensile tester designed for in-
situ usage in the tomograph, the obtained loading curves are more scattered than
when the same experiments where performed with the tensile tester in the laboratory
at Tetra Pak in cf. Figure 4.6. This has to do with the equipment used. A lower
stiffness of the equipment will be seen as a larger displacement for the same stress
when compared to a stiffer equipment. Another factor that could affect the result is

61

that the displacement rate differed from the tests performed in the laboratory at Tetra Pak, (see Section 3.2). The manual tightening of the clamps may also have affected the results, since it is hard to get exactly the same pressure between the clamps all the time. There might also be some sliding due to grips not being tightened properly. This should however not affect the failure strength. As described previously, also the climate can have an impact on the results since the experiments performed at Lund University were performed in an uncontrolled environment leading to possible changes of the relative humidity during the experiments. However, after normalisation the impact of the environment does not affect the result.

To minimise the impact of these possible error sources in the experiments performed at Lund University, certain changes to the equipment or the methods used are suggested. The tensile equipment could be constructed of stiffer components to get a more correctly measured displacement. Another solution would be to use the images from the tomograph to measure the displacement instead of the strain-gauge, and hence avoid impact of compliance of the equipment on the measured displacement. Furthermore, the displacement rate could be controlled in a similar way as the experiments at Tetra Pak and the tightening of the clamps could be performed using a torque wrench to get more consistent conditions for the experiments.

By using the software Fiji, it was possible to measure the thickness of the specimen at each holding point. By doing this it was observed that initially, between holding points 1 to 4, a minor thickness increase existed between each holding point. The rate of thickness increase appeared to be linearly, but more holding points in closer proximity to each other is needed to verify this. Between holding points 4 and 5 the specimen dilated rapidly and after failure strength the thickness increase slowed down to a rate close to the initial rate, which seems reasonable since widening of the localised failure zone is present and the specimen is not strained in the same sense any more.

One explanation for the behaviour regarding the thickness increase might be that, in the beginning of the loading, the fibres and the fibre-to-fibre connections are elongated resulting in a moderate thickness increase. When further strained, the connections are not able to hold any more, hence delamination occurs within the material giving the sudden increase in thickness. This theory is validated by investigating the images in Figure 4.16, where no voids are visible at the first 4 holding points. When reaching holding point 5 dark voids are visible, indicating delamination.

By comparing short-span tensile experiments performed with pre-delaminated and not pre-delaminated samples, it was proven statistically that the mean failure strength, fracture energy and maximum slope of the cohesive relation was the same (except for the failure strength in CD), independent of delamination for both MD and CD. Hence, delamination does not have any effect on the in-plane failure behaviour and initialisation of the localised failure zone.

To further analyse the mechanisms and movement of the internal structure, strain fields were constructed using DVC. It was not known if this method would work on paperboard since DVC only works if it is possible to determine a unique structure for each voxel. From the result it was proven that it is possible to use DVC on paperboard.

Beginning with the normal strains in CD, ϵ_{CD}, strain localisation at the notches was observed. The reason for higher strains at the notches is due to stress concentrations. Higher strains at the notches can also be seen for example in Figures 4.23 and 4.27, which indicates that the stress concentration at the notches affect strains in all normal directions. No other clear patterns were visible in the ϵ_{CD}-fields, which was expected since the load was applied in MD and should therefore not have a large impact on strains in CD.

Continuing with the normal strains in ZD, ϵ_{ZD}, it should be noted that the strains were already present between holding points 1 and 2. This matches the thickness increase observed in Figure 4.16. It appears that the strains are more focused at the centre of the sample in the thickness direction. This observation and the reason behind it needs to be investigated further, but it might be related to the manufacturing process. Since the strains are localised in the middle already between holding points 1 and 2, there is some dilation occurring there, which may indicate that it is a risk that delamination occurs even at low loads. However, as was proven with the short-span tensile tests with pre-delaminated samples, delamination does not have a large impact on the failure strength. With this said, the similarities between the strain localisation in ZD and the path of the localised failure zone are noticeable and seems to be connected.

The normal strains in MD appear to be relatively homogeneous, with localised zones of higher strain that evolve in a small rate during increased loading. It appears that when the localised failure zone evolves, it chooses one of the zones with higher strain and propagate through only that zone. Short-span tensile tests where multiple localised failure zones, instead of one single localised failure zone, were present in the same sample has been observed, but is uncommon. This validates the authors' theory that the localised failure zone chooses one zone with higher strain to propagate in. The authors' theory is therefore also that the strains in the loading direction have the biggest impact on both the localisation initiation and how the localised failure zone evolves.

After failure, the strains in MD are localised to the localised failure zone and the strains outside of the failure zone are small compared to before failure. This implies that all energy goes to the localised failure zone while the rest of the sample is relaxed, see Section 2.1.3.

Regarding the shear strains, one interesting part is the ϵ_{ZDMD}-field between holding points 1 and 2 (in view A image γ in Figure 4.29), where more positive strains are observed at the bottom compared to at the top. The reason might be that the sample became vertically aligned when the loading started due to the design of the equipment

used. Between later holding points it looks like the higher strains in the ϵ_{ZDMD}-field are focused between the notches as expected due to the smaller cross-sectional area.

As previously discussed, comparison between the actual magnitude of strains between different holding points should be treated with caution, due to the different total displacement between each holding point. However, by comparing the ϵ_{ZDMD}-field in Figure 4.31 with the ϵ_{ZDMD}-field in Figure 4.32 it can be seen that the strains differ a lot. The conclusion from this can be that the shear strains in this direction become much more significant after localisation of the failure zone. This may imply that the shear strains can be the reason that the localised failure zone is not perpendicular to MD.

5.2 Conclusions

In this Master's Thesis, tensile experiments have been performed on a one ply paperboard to analyse size effects. X-ray tomography has also been used, together with digital volume correlation to further analyse the material response under tensile loading.

From the experiments, it was concluded that the cohesive failure is independent of the sample geometry, after normalisation has been performed. From the 3D-images provided by the x-ray tomograph, a thickness increase was observed immediately after loading was applied. Close to fracture, a large, sudden, thickness increase occurred which probably is due to delamination, but during the Thesis work it was showed that delamination does not affect the cohesive failure.

The usage of digital volume correlation on the tomograph images proved to be an analysing method well suited for paperboard, and provided information about how the paperboard deformed as well as how the internal structure evolved under tensile loading. The strains in the specimen were localised in zones of higher strains in the MD-direction under tensile loading, which probably caused the initiation and propagation of the localised failure zone. The strains in the thickness direction showed that the strains localised in the centre of the sample in ZD-direction, this might have to do with the manufacturing process of the paperboard. Furthermore, shear strains increased rapidly when the failure zone initialised, which indicates that shear strains can be the reason for the diagonal propagation of the localised failure zone.

5.3 Further work

To get a more solid statistical basis to confirm the results and the developed theories more experiments need to be performed. It is also of interest to perform tomographic experiments in other directions than MD, to get more knowledge about the material under more general loading conditions.

In this Master's Thesis only a one ply paperboard has been analysed. Performing tomographic experiments on different types of paperboards would be of interest to increase the understanding of what is going on in different types of paperboards when they are subjected to tensile loading.

Regarding the test procedure, shorter intervals between the holding points are needed to be able to analyse the material even better. This would be time consuming, but hopefully it would result in an even better knowledge about paperboard and how it behaves when it is subjected to tensile loading.

Bibliography

[1] Marin, G. (2014). Master Thesis, *In-plane fracture of paperboard*, Department of Solid Mechanics, Royal Institute of Technology, Stockholm, Sweden.

[2] Gross, D., Seelig, T. (2011), *Fracture mechanics with an introduction to micromechanics*, Springer-Verlag Berling Heidelberg, Germany.

[3] Tryding, J. (1996). Doctoral Thesis, *In-plane fracture of paper*, Division of Structural Mechanics, Lund University, Lund, Sweden.

[4] Mäkelä, P. (2002). *On the fracture mechanics of paper*, Swedish Pulp and Paper Research Institute, Stockholm, Sweden.

[5] Borgqvist, E., Tryding, J. (2017), *From fiber, pulp, paperboard to packages*, Lecture presented at; 2017; Lund University.

[6] Tryding, J., Marin, G., Nygårds, M., Mäkelä, P., Ferrari, G (2017), *Experimental and theoretical analysis of in-plane cohesive testing of paperboard*, International journal of damage mechanics, Lund, Sweden.

[7] Borgqvist, E. (2016). Doctoral Thesis, *Continuum modelling of the mechanical response of paper-based materials*, Department of Construction Sciences, Lund University, Lund, Sweden.

[8] Baum, G.A. (1984), *The elastic properties of paper: a review*, The institute of paper chemistry, Appleton, USA.

[9] Stenberg, S. (2002). Doctoral Thesis, *On the Out-of-Plane Mechanical Behaviour of Paper Materials*, Department of Solid Mechanics, Royal Institute of Technology, Stockholm, Sweden.

[10] Buffiere, J.-Y., Maire, E., Adrien, J., Masse, J.-P. and Boller, E. (2010), *In situ experiments using X ray tomography: An attractive tool for experimental mechanics*, Society of experimental mechanics, France.

[11] Håkansson, O. (2014). Master Thesis, *Experimental and numerical analysis of out-of-plane shear of paperboard*, Division of Solid Mechanics, Lund University, Lund, Sweden.

[12] Tryding, J., Ristinmaa, M. (2017). *Normalisation of cohesive laws for quasi-brittle materials*, Division of solid mechanics, Lund University, Lund, Sweden.

[13] Hagman, A., Nygårds, M. (2012), *Investigation of sample-size effects on in-plane tensile testing of paperboard*, KTH, Stockholm, Sweden.

[14] Weibull, W. (1939), *A statistical theory of the strength of materials*, Ingenjörsvetenskapsakademin, Royal technical university, Stockholm, Sweden.

[15] Moreton, R. (1968), *The effect of gauge length on the tensile strength of R.A.E. carbon fibres*, Royal Aircraft Establishment, Great Britain.

[16] Rolland du Roscoat, S., Bloch, J-F., Thibault, X. (2005), *Synchrotron radiation microtomography applied to investigation of paper*, Institute of Physics , Grenoble, France.

[17] Mark, R., Habeger, C., Borch, J., Bruce-Lyne, M. (2002), *Handbook of physical testing of paper*, Empire State , New York, USA.

[18] Gabrielsson, A., Granlöf, L., Trost, T. (2017). *Moisture sensitivity of cohesive in-plane properties of paperboards*, Prpject 1.7, Innventia Report No.:877, Stockholm, Sweden.

[19] Gabrielsson, A., (2017), *Optical methods to study deformation mechanisms during short tensile testing*, Report no.:892, Innventia Research Programme.

[20] Persson, K., Danelius, M. Master Thesis, *Mechanical properties of crease*, Division of Structural Mechanics, Lund University, Sweden.

[21] Murata, H. (2012). Master Thesis, *Rheology - Theory and Application to Biomaterials*, Department of Prosthetic Dentistry, Nagasiki University, Japan.

[22] X-ray computed tomography. Science education resource centre, Carleton college [updated 16 May 2017; cited 21 September 2017]. Available from: https://serc.carleton.edu/research_education/geochemsheets/techniques/CT.html

[23] Brunke, O. (1996). Doctoral Thesis, *Comparison between x-ray tube based and synchrotron radiation based µCT*, GE Sensing & inspection Technologies GmbH, Wunstorf, Germany.

[24] Hall, S.A., Viggiani, G., Romero, E., (2012). *Advanced experimental techniques in geomechanics*, The Alliance of Laboratories in Europe for Research and Technology.

[25] Schindelin, J., Arganda-Carreras, I., Frise, E. et al. (2012), *Fiji: an open-source platform for biological-image analysis*, Nature methods 9(7): 676-682, PMID 22743772, doi:10.1038/nmeth.2019 (on Google Scholar).

[26] Tudisco, E., Andò, E., Cailletaud, R., Hall, S. (2017) *TomoWarp2: A local digital volume correlation code*, Department of Construction Sciences, Lund University, Sweden. University Grenoble Alpes, France.

[27] Paired Sample T-Test. Statistics Solutions [updated 2017; cited 20 December 2017]. Available from: http://www.statisticssolutions.com/manova-analysis-paired-sample-t-test/

Appendix

Appendix A

Relaxation experiments

The relaxation experiments were performed in the laboratory at Tetra Pak and a similar setup like the one used for the short-span tensile tests performed in the same laboratory was also used for the relaxation experiments. The exact same testing machine and clamps were used, and the specimens were prepared in the same way. However the settings of the experiments altered. The same displacement rate was used, but the sampling rate was set to 10 ms. The reason for this was that the tests was going to take about 80 minutes each compared to the short-span tests that took about thirty seconds. Note that these experiments were only performed on the notched specimens, as they were the ones used in the tomograph.

A number of two points, one before and one after failure strength were chosen for each experiment. The selected points are displayed as green dots in Figure A1. The locations of the points were chosen before- and after failure strength, where initiation of the failure zone was expected to occur. It should be noted that the location of the points in Figure A1 differs slightly between different tests.
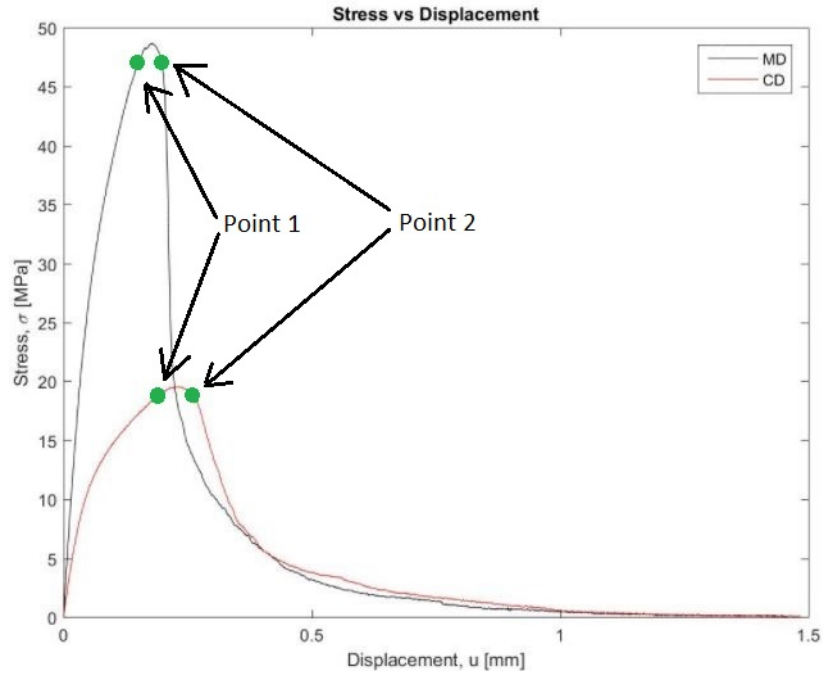
Figure A1: Selected points used in the relaxation tests performed on paperboard at Tetra Pak.

It should be noted that the relaxation tests done in the laboratory at Tetra Pak would differ compared to if relaxation tests would have been performed in uncontrolled environment using the tensile machine that was used in the tomograph. This is mainly due to different displacement rates for the different equipments, however, also temperature and moisture content differences can have an impact. Even though the conditions differ the relaxation tests done in the laboratory at Tetra Pak gave an approximative result of the time needed between tensile test stop and tomograph start when performing the experiments in the tomograph.

Point 1 in Figures A1, A2 and A3 corresponds to tests before failure strength, and point 2 corresponds to tests after failure strength. Due to noisy data all the graphs showed in this section were denoised using a moving average filter in Matlab.

In Figures A2 and A3 the normalised stress as a function of time is shown for both MD and CD respectively.
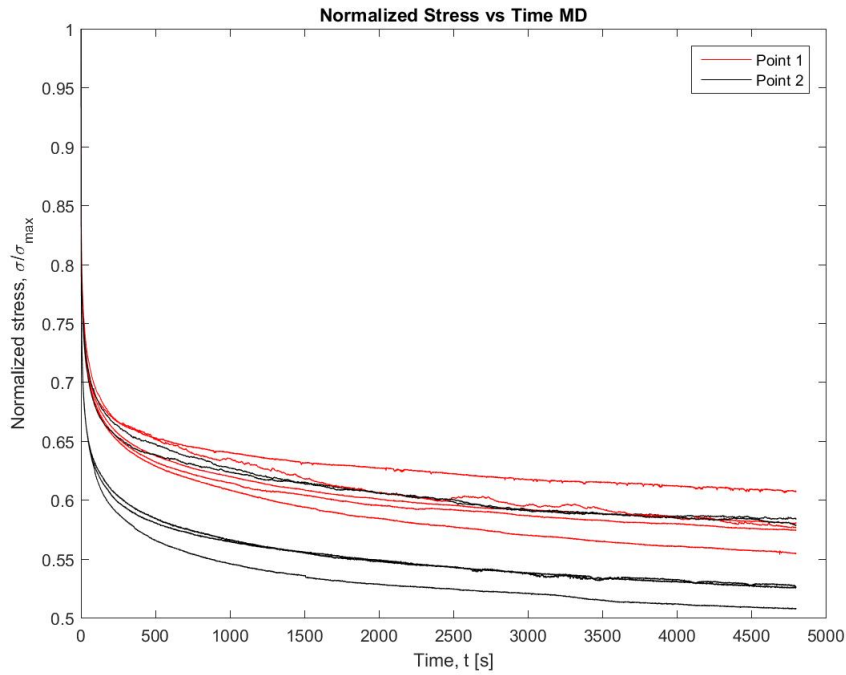
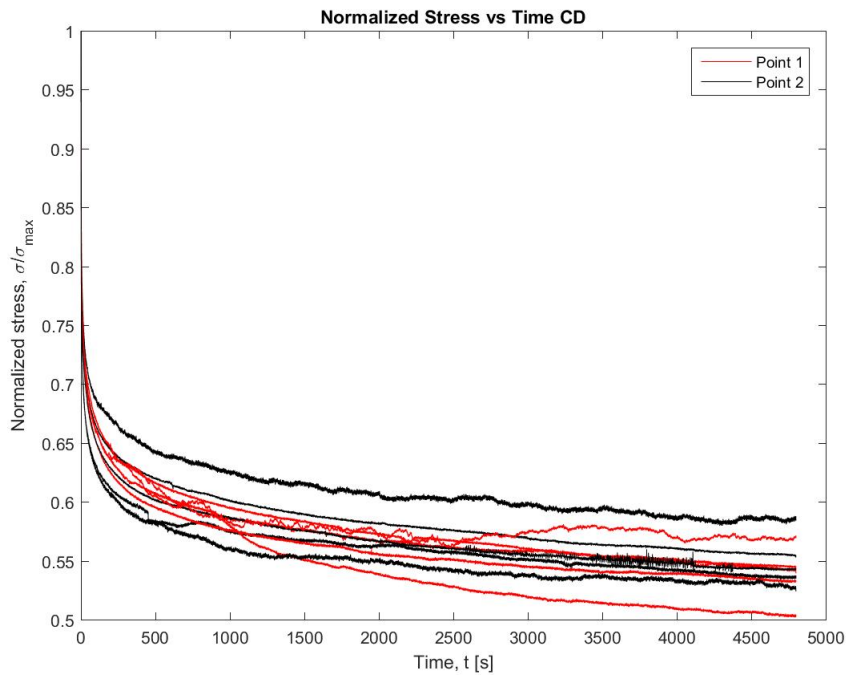Figure A2: Normalised stress-time curves for paperboard samples in MD.

Figure A3: Normalised stress-time curves for paperboard samples in CD.

In these graphs it can be seen that the rate of relaxation decreases over time. One outlier exists in CD, where the stress increases in the end of the experiment. This result is unreasonable, and should be ignored. In the first ten minutes the drop in

stress is large compared to later when the sample starts to reach equilibrium as was discussed in Section 2.1.8. From figures A2 and A3 it can be seen that the sample structures are not in equilibrium even though the displacement is held constant.

In MD the curves from point 1 (before failure) is rather consistent, the stress lowers to approximately 60-65 % of the stress acting at the start of the relaxation tests. The result for point 2 (after failure) is more inconsistent. Two of the curves dropped the same amount as for the curves before failure, while three relaxed to about 50-55 % of the original stress. However the rate of relaxation in the beginning is similar.

In CD there are no obvious difference between before and after the failure strength (i.e point 1 and 2). The stress lowers to about 55-60 % of the stress acting at the start of the relaxations tests. The rate of relaxation appears to be similar as well.

The relaxation experiments resulted in knowledge about the time needed for the relaxation rate to slow down from the initially high rate to a significantly lower rate. From these experiments it was noted that the behaviour regarding MD after failure was inconsistent. To further investigate the relaxation behaviour, and get more statistically proven results, more experiments needs to be performed. Furthermore, the noise for the relaxation experiments were presumably caused by the fact that the machine was located on a shared workbench, and hence other people were performing experiments close to the machine during the experiments. A slight movement of the bench creates vibrations that are seen as jumps in the graphs.

For the tomograph experiments, it will take approximatively one hour for the tomograph to construct an image of the material and an extra twenty minutes is needed to account for the time between the stop of the tensile machine and the start of the tomograph. Hence, the time for which the relaxation was investigated was 80 minutes.

Appendix B

Table B1: Settings used in the DVC program.

Hold p.	Search Window						Correlation Window						Node Spacing		
	x		y		z		x		y		z		x	y	z
1-2	-20	20	-20	20	-20	20	-10	10	-10	10	-10	10	6	6	6
2-3	-20	20	-20	20	-20	20	-10	10	-10	10	-10	10	6	6	6
3-4	-20	20	-20	20	-20	20	-10	10	-10	10	-10	10	6	6	6
4-5	-25	10	-15	60	-15	50	-10	10	-10	10	-10	10	6	6	6

Appendix C
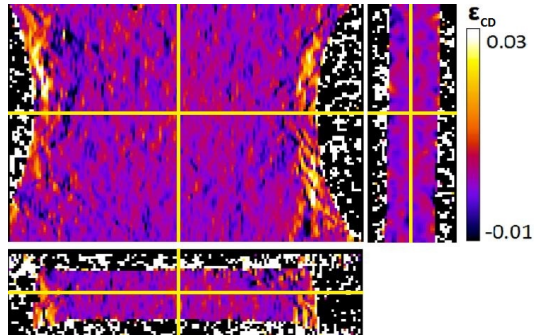
Strain fields

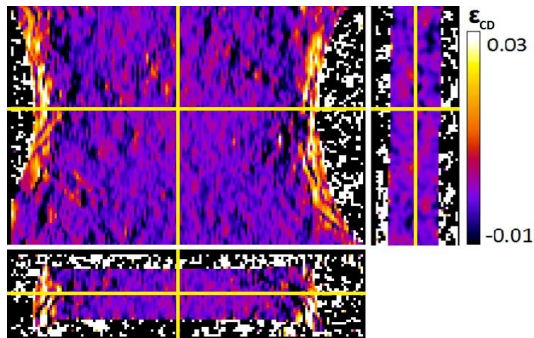Figure C1: ϵ_{CD}-field between holding points 1 and 2.

Figure C2: ϵ_{CD}-field between holding points 2 and 3.